Four-way coupled simulations of small particles in turbulent channel flow: the effects of particle shape and Stokes number

F. Zhao,[1] W.K. George,[2] and B.G.M. van Wachem[1, a)]

[1)] *Division of Thermofluids, Department of Mechanical Engineering, Imperial College, London, SW7 2AZ, UK*

[2)] *Department of Aeronautics, Imperial College, London SW7 2AZ, UK*

(Dated: 6 July 2015)

This paper investigates the effects of particle shape and Stokes number on the behaviour of non-spherical particles in turbulent channel flow. Although there are a number of studies concerning spherical particles in turbulent flows, most important applications occuring in process, energy and pharmaceutical industries deal with non-spherical particles. The computation employs a unique and novel four-way coupling with the Lagrangian point-particle approach. The fluid phase at low Reynolds number ($Re_\tau = 150$) is modelled by DNS, while particles are tracked individually. Inter-particle and particle-wall collisions are also taken into account. To explore the effects of particles on the flow turbulence, the statistics of the fluid flow such as the fluid velocity, the terms in turbulence kinetic energy equation, the slip velocity between the two phases and velocity correlations are analysed considering ellipsoidal particles with different inertia and aspect ratio.

The results of the simulations show that the turbulence is considerably attenuated, even in the very dilute regime. The reduction of the turbulence intensity is predominant near the turbulence kinetic energy peak in the near wall region, where particles preferentially accumulate. Moreover, the elongated shape of ellipsoids strengthens the turbulence attenuation. In simulations with ellipsoidal particles, the fluid-particle interactions strongly depend on the orientation of the ellipsoids. In the near wall region, ellipsoids tend to align predominantly within the streamwise (x) and wall-normal (y) plane and perpendicular to the span-wise direction, whereas no preferential orientation in the central region of the channel is observed. Important conclusions from this work include: the effective viscosity of the flow is not affected, the direct dissipation by the particles is negligible, and the primary mechanism by which the particles affect the flow is by altering the turbulence structure around the turbulence kinetic energy peak.

Keywords: dispersed multiphase flow; non-spherical particles; turbulent channel flow

[a)]Electronic mail: berend.van.wachem@gmail.com

I. INTRODUCTION

Small solid particles suspended in turbulent carrier fluids are commonly found in industrial applications such as paper making, fuel combustion processes, cyclones, as well in environmental phenomena, such as sand storms and the spread of soot particles, to name a few. In these gas-solid flows, complex interactions between dispersed particles and fluid flows make the phenomena of dispersed two-phase flows much more complex than single-phase flows. In the literature, gas-solid wall-bounded flows have been extensively studied experimentally[1–4] and numerically[5–7]. Most of these research papers investigated flows with spherical particles. However, particle shapes in realistic applications are usually not confined to spheres. Therefore, the understanding of gas-solid multiphase flows with non-spherical particles is of growing interest. Since the fluid-particle interactions are significantly influenced by the particle shape and orientation, the dynamics of non-spherical particles in turbulent flows are quite complicated and difficult to predict. There are relatively few papers concerning non-spherical particles. Our numerical study focuses on one such challenging area, fiber-shaped ellipsoidal particles with different Stokes numbers in a turbulent channel flow. The results are compared to flows with spheres to explore the effects of elongated particle shape and Stokes number on both the particles and the fluid behaviour.

In recent decades, ellipsoidal particles dispersed in a turbulent channel flow have been numerically studied[8–14]. The ellipsoids in these studies are referred to as spheroids with two equal minor axes, and this type of ellipsoid is also adopted in the present work. Among those papers, Zhang *et. al.*[12] was the first to apply Direct Numerical Simulation (DNS) to solve fluid channel flow with spheroids. The DNS approach provides the most accurate prediction of the fluid behaviour and provides a better insight to the physics of the flow problem. Following Zhang's work, Mortensen *et. al.*[10,11] and Marchioli *et. al.*[9] reported the statistics of ellipsoids with different aspect ratio and inertia. Similar to spherical particles, elongated ellipsoids also tend to accumulate in the near wall region and preferentially concentrate in the regions of low-speed and high strain.

Most of these previous papers[9,11,12], applied one-way coupling to model the gas-solid channel flow with ellipsoidal particles, and the effects of discrete particles on the fluid flow, particle-particle and particle-wall collisions were ignored. However, at which level of particle volume fraction or mass loading the collision effect on both phases becomes significant is

still uncertain for non-spherical particles, and inter-particle and particle-wall collisions can strongly affect the dynamics of non-spherical particles. Moreover, the presence of dispersed solid particles may influence the flow turbulence, even in very dilute flows. Therefore, these fluid-particle and particle-particle interactions play an important role in gas-solid channel flow with non-spherical particles. To perform more realistic simulations of gas-solid channel flow, this paper uses the four-way coupling to fully resolve the particle-fluid and particle-particle interactions, as well as including the effects of particles on fluid flow, the effect of the fluid flow on particles, particle-particle and particle-wall collisions.

In the literature, several numerical approaches for modelling gas-solid flows have been reviewed by Balachandar and Eaton[15]. Among these approaches, the Lagrangian point-particle approach developed by Crowe, Sharma, and Stock[16] has been extensively applied[6,17–20], and also used in this study. In this approach, solid particles are tracked individually, and their properties, such as position, mass momentum and energy of individual particle, are determined by Newton's second law. The particle size has to be much smaller than Kolmogorov length scale for the point-source approximation to be valid.

In this paper, the effect of the fluid flow on dispersed particles is described by modelling the hydrodynamic drag forces and torques, which depend on the particle shape and Reynolds numbers. For non-spherical ellipsoids in a viscous fluid, drag interactions were derived by Jeffery[21] and Brenner[22,23], which approximated drag forces and torques under the creeping flow condition. Further theoretical work of drag on ellipsoidal particles was reported in Gallily *et. al.*[24]. Drag models based on these studies provide good approximations for the hydrodynamic force and torque on ellipsoids in a turbulence flow with very small Reynolds number, and have been applied in the previous studies[9,11,12,14,25], as well as in the current work. On the other hand, the effects of particles on the fluid flow can be summed and added into the fluid momentum equation as a source term. Andersson and Zhao *et. al.*[13,25] proposed an torque-coupling to include the drag torque on the fluid flow in their simulations. Due to the small particle size in our simulations, the effect of the drag torque on the fluid flow is ignored, and only the drag force is taken into account in this study. To detect and resolve all inter-particle and particle-wall contact collisions, a soft-sphere collision model is applied herein. Unlike one-way coupling studies[9,11,12] that only discussed the statistics of particles, the current study which applies the four-way coupling can investigate the effects of particle shape and Stokes number on both the fluid flow and particles.

One difficulty when modelling the dynamics of non-spherical particles is to accurately represent the orientation and rotation of non-spherical particles. In most previous studies[9,11,12], the rotation and orientation of ellipsoids are described by unit Quaternions in conjunction with the corresponding rotation matrices which can explicitly transform variables to the various co-ordinate frameworks. In this study, only unit Quaternions are used without the necessity of the corresponding rotation matrices. To achieve this, a new Quaternion equation relating tensor variables in different frameworks is put forward. Furthermore, a novel Quaternion integration method[26] is proposed for accurately updating unit Quaternions. Using only Quaternion multiplications, this algorithm avoids the numerical errors caused by the addition or subtraction of Quaternions present in the other integration algorithms, so it more precisely predicts the rotational motion and orientation of non-spherical particles.

The current paper adopts the same computational domain and fluid properties as those in Marchioli *et. al.*[6,9]. For the sake of simplicity, several assumptions are made. First, no gravity. Second, effects of Brownian motion are negligible. And third, the particle sizes are assumed smaller than the Kolmogorov microscale so they can be treated as point particles[16,27]. The particle properties are varied by changing the particle inertia and aspect ratio. In the literature, the flow turbulence modulation due to the presence of solid particles is widely discussed and analysed by comparing the statistics of fluid velocities, in particular, the mean flow velocity, the fluid root mean square (RMS) velocity and the Reynolds stresses for the different particle properties. However, more complex information on the flow turbulence, such as the fluid flow turbulence production, the fluid flow dissipation rate and the dissipation rate caused by particles, are rarely discussed for gas-solid channel flow, especially for flows with non-spherical particles. This paper will directly analyse these statistics of the fluid flow to explore the effects of particle shape and Stokes number on the flow turbulence. In the papers Marchioli, Fantoni, and Soldati[9], Mortensen *et al.*[11], Zhang *et al.*[12], the orientation of ellipsoidal particles are represented by the mean absolute cosine values. However, averages of the non-linear cosine function may not accurately describe the orientation of the particles. Therefore, the angles between the major axis of ellipsoidal particles and the axes of the Eulerian framework are used to represent the orientation of non-spherical particles, as well as the angles of the major axis of ellipsoids projected on three planes perpendicular to the axes of the Eulerian framework. The distribution of these orientation angles in the near wall and central regions are analysed to investigate the particle orientations in the channel

flow.

The aim of this work is to investigate not only the behaviour of ellipsoidal particles in a turbulent channel flow but also the effect of the particle shape and Stokes numbers on the flow turbulence. The paper is organised as follows. In section 2, the governing equations of the fluid and particle phases are put forward, and the novel Quaternion equations are then proposed. After that, the four-way couplings are fully described. Section 3 specifies the simulation settings. In section 4, the statistics of the fluid flow and particles are presented and discussed. Finally, some conclusions are drawn in section 5.

II. METHODOLOGY

In this section, the governing equations of the fluid flow and the particles are formulated, and the four-way coupling is specified, including the fluid effects on particles, the inverse particle effects on the fluid flow, particle-particle and particle-wall collisions.

A. Fluid flow

The Eulerian fluid flow is determined in the framework of DNS, and assumed as an incompressible, isothermal and Newtonian fluid flow. The governing equations for the fluid phase are the continuity equation:

$$\frac{\partial u_i^f}{\partial x_i} = 0 \tag{1}$$

and the Navier-Stokes equation:

$$\frac{\partial u_i^f}{\partial t} + u_j^f \frac{\partial u_i^f}{\partial x_j} = -\frac{1}{\rho^f}\frac{\partial p}{\partial x_i} + \nu^f \frac{\partial^2 u_i^f}{\partial x_j^2} + \Pi_i + \frac{1}{\rho^f}\nabla P_i \tag{2}$$

where u_i^f is the fluid velocity, ρ^f is the fluid density, p is the kinetic pressure, ν^f represents the fluid kinematic viscosity and the source term Π_i describes the momentum exchange between the particles and the fluid phase. A mean pressure gradient ∇P_i drives and maintains the channel flow, given as

$$\nabla P_1 = \frac{\rho^f {\nu^f}^2 Re_\tau^2}{h^3} \tag{3}$$

where h is the half channel height, and $Re_\tau = u_\tau h/\nu^f$ is the friction Reynolds number. The imposed pressure gradient fixes the wall shear stress (and u_τ), so any changes at the very near wall show up only because of changes in kinematic viscosity. If present, drag reduction would show up as an increase in centerline velocity. In this study, this Reynolds number is fixed at 150 for all simulations, and friction velocity $u_\tau = \sqrt{\tau_0/\rho^f}$ in Re_τ is determined by the mean shear stress at the wall, τ_0. In the above equations, the superscript f on the variables indicates these variables for the fluid phase, and the subscript i represents the $i^{\text{th}}(i = 1,\ 2 \text{ or } 3)$ component, where the Einstein convention of summation over repeated indices is assumed.

B. Rigid particle dynamics

The motion of a rigid particle can be divided into translational and rotational motion. To precisely and conveniently describe the motion of non-spherical particles, two Cartesian co-ordinate frameworks are employed: body-space and world-space, as depicted in Fig. 1. In world space, the axes are fixed in the origin of the initial Cartesian framework which corresponds to the Eulerian fluid framework, *see* Fig. 1(b). In body-space, the axes are aligned with the principle axes of a particle, and the framework origin is fixed on the particle center of mass. For all variables in body space, the superscript b will be used, whereas variables without this superscript mean they are in world space.

1. Particle translational dynamics

The translational motion of particles is governed by the Newton's second law in world space,

$$\sum \boldsymbol{F} = m\frac{d\boldsymbol{u}^p}{dt} \tag{4}$$

where $\sum \boldsymbol{F}$ is the resultant external force on the particle, m is the particle mass, and $\boldsymbol{u}^p$ represents the particle translational velocity. Due to the applied assumptions and large particle-fluid density ratio, several forces in the Basset-Boussinesq-Oseen (BBO) equation[28,29] are neglected in this work, and only hydrodynamic drag, the pressure gradient and collision forces are included in $\sum \boldsymbol{F}$.

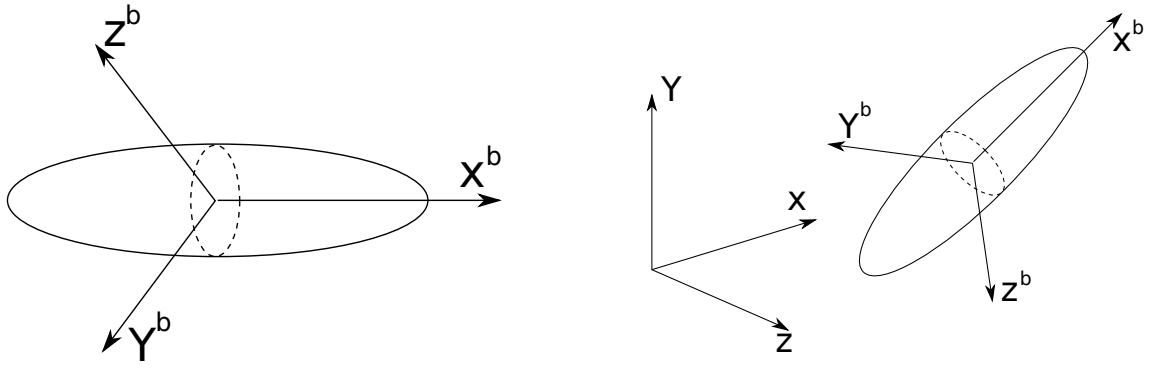

(a) Body space (b) World space

FIG. 1. (a) Body space and (b) World space co-ordinates. The x^b axis of the body-space co-ordinate system always aligns with the major-axis of the ellipsoidal particle, whereas the world-space co-ordinates remain fixed in space and time.

The linear velocity $\boldsymbol{u}^p$ and position of particles are computed by using a second order Verlet scheme[30]. For spherical particles, the translational motion can fully describe their dynamics. However, the orientation of a non-spherical particle can considerably influence the effects of the fluid, *i.e.* the hydrodynamic drag force and torque, on the particle so that the rotational motion of non-spherical particles is also required to be resolved.

2. Particle rotational dynamics

Equations for representing the particle rotation are complex in world space, and the most common way is to solve these equations in body space. The governing equation for rotation is then expressed as:

$$\dot{\boldsymbol{\omega}}^b = \overline{\overline{I}}^{b\,-1}(\boldsymbol{T}^b - \boldsymbol{\omega}^b \times \boldsymbol{L}^b) \tag{5}$$

where $\overline{\overline{I}}^b$ is the constant particle inertia tensor, $\boldsymbol{T}^b$ is the torque acting on the particle, $\boldsymbol{\omega}^b$ represents the particle angular velocity in body space, and $\boldsymbol{L}^b = \overline{\overline{I}}^b \boldsymbol{\omega}^b$ is the angular momentum. The tensor $\overline{\overline{I}}^b$ depends on the orientation of the ellipsoid in body space. In this work, the minor axes of the ellipsoid are aligned with the y^b and z^b axes of body space, while the major axis matches the x^b axis of body space, *see* Fig. 1. This arrangement enables the

off-diagonal components in $\overline{\overline{I}}^b$ to be zero, and $\overline{\overline{I}}^b$ is given as

$$\overline{\overline{I}}^b = \begin{pmatrix} \frac{2ma^2}{5} & 0 & 0 \\ 0 & \frac{(1+\lambda^2)ma^2}{5} & 0 \\ 0 & 0 & \frac{(1+\lambda^2)ma^2}{5} \end{pmatrix} \tag{6}$$

where a and λ are the length of semi-minor axis and aspect ratio of the ellipsoid, respectively.

3. Rotation operator: unit Quaternion

For non-spherical particles, the representation of the rotation requires a rotation operator. There are three most commonly used operators to describe rotation dynamics: Euler angles, rotation matrices, and unit Quaternions. Applying the former two can give rise to gimbal lock and singularity problems[31], and hence the latter, unit Quaternions, are used in this study. A Quaternion is defined as

$$q = [q_0, \boldsymbol{q}] \tag{7}$$

where q_0 is a scalar number, and $\boldsymbol{q} = [q_1,\ q_2,\ q_3]$ is a vector. In dynamic systems, a general Quaternion cannot only rotate a vector, but also scale the length of the vector[32]. To describe rotation without scaling, the length of Quaternions must always be 1, given as

$$|q| = \sqrt{q_0^2 + q_1^2 + q_2^2 + q_3^2} = 1 \tag{8}$$

Furthermore, the Quaternion multiplication product is required, which can be defined as:

$$pq = [p_0 q_0 - \boldsymbol{pq}, p_0\boldsymbol{q} + q_0\boldsymbol{p} + \boldsymbol{p} \times \boldsymbol{q}] \tag{9}$$

where p and q are Quaternions. A vector $\boldsymbol{v}$ rotated by a pair of unit Quaternions is defined by

$$\boldsymbol{v}'' = qvq^{-1} \tag{10}$$

where $q^{-1} = [q_0, -\boldsymbol{q}]$ represents the conjugation of q, and vector $\boldsymbol{v}$ is interpreted as the Quaternion, $[0, \boldsymbol{v}]$.

Relevant previous studies[9,11,12] also applied unit Quaternions to represent rotation, and corresponding rotation matrices were adopted to transform vector and tensor variables among different co-ordinate frameworks. Obtaining these matrices from unit Quaternions requires significant additional computations. This can give rise to inaccuracies or instability, and it

also requires more computational time and memory. To avoid these drawbacks, this study uses unit Quaternions to determine the variable transformation directly, instead of rotation matrices. Although vector variables can be easily rotated by using Equation 10, the Quaternion expression for transforming tensors is more complex. This is derived in Zhao and van Wachem[26], and briefly described as follows. A second order tensor $\overline{\overline{M}}$ can be considered as three sequence column vectors $\overline{\overline{M}}_{123}$, of which the rotation can be defined by

$$\overline{\overline{M}}'_{123} = q\overline{\overline{M}}_{123}q^{-1} \tag{11}$$

Based on this equation, the transformation of a tensor by unit Quaternions is expressed as

$$\overline{\overline{M}}'' = (q(q\overline{\overline{M}}q^{-1})^T q^{-1})^T \tag{12}$$

which is equivalent to the following rotation matrix expression,

$$\overline{\overline{M}}'' = \overline{\overline{R}}\,\overline{\overline{M}}\,\overline{\overline{R}}^{-1} \tag{13}$$

where $\overline{\overline{R}}$ is the corresponding rotation matrix. By applying Quaternion equations 10 and 12, this study avoids the necessity of rotation matrices all together.

4. The integration of unit Quaternions: predictor-corrector direct multiplication (PCDM) method

In the literature, most integration methods for updating unit Quaternions are performed based on Taylor expansions[11,30,33,34]. Unfortunately, these algorithms cannot preserve the unit length of the rotation operators; therefore, the Quaternions must be re-normalized after each particle time-step. Although the re-normalization procedure ensures that the Quaternions keep their unit lengths, the inherent relationship among the 4 components in a Quaternion is affected and leads to inevitable errors in rotation angle. To avoid this, this study employs a new algorithm PCDM method[26] to integrate unit Quaternions. This method implicitly preserves the length of unit Quaternions without re-normalization. The unit Quaternion at the next time-level $n+1$ is determined by

$$q_{n+1} = \tilde{q}_{n+1}q_n \tag{14}$$

where the unit Quaternion $\tilde{q}_{n+1}$ represents the rotation from time-level n to $n+1$ and is defined by

$$\tilde{q}_{n+1} = \left[\cos\left(\frac{|\boldsymbol{\omega}_{n+\frac{1}{2}}|\delta t}{2}\right), \sin\left(\frac{|\boldsymbol{\omega}_{n+\frac{1}{2}}|\delta t}{2}\right)\frac{\boldsymbol{\omega}_{n+\frac{1}{2}}}{|\boldsymbol{\omega}_{n+\frac{1}{2}}|}\right] \tag{15}$$

where δt represents the time-step, and $|\boldsymbol{\omega}_{n+\frac{1}{2}}|$ is the length of angular velocity $\boldsymbol{\omega}_{n+\frac{1}{2}}$. In Equation 14, the multiplication product between two unit Quaternions guarantees the unit length of the results q_{n+1}. In the PCDM algorithm, the angular velocity of particles and unit Quaternions are approximated by a predictor-corrector method. Firstly, the external torque $\boldsymbol{T}_n$ and angular velocity $\boldsymbol{\omega}_n$ of a particle are transformed from world space to body space using Equation 10, and temporal $\boldsymbol{\omega}^b_{n+\frac{1}{4}}$ and $\boldsymbol{\omega}^b_{n+\frac{1}{2}}$ in body space are then computed by the first order Euler algorithm. After that, a predictor Quaternion $q''_{n+\frac{1}{2}}$ can be determined by

$$q''_{n+\frac{1}{2}} = \left[\cos\frac{\|\boldsymbol{\omega}_{n+\frac{1}{4}}\|\delta t}{4}, \sin\frac{\|\boldsymbol{\omega}_{n+\frac{1}{4}}\|\delta t}{4}\frac{\boldsymbol{\omega}_{n+\frac{1}{4}}}{\|\boldsymbol{\omega}_{n+\frac{1}{4}}\|}\right] q_n \tag{16}$$

Applying $q''_{n+\frac{1}{2}}$, $\boldsymbol{\omega}^b_{n+\frac{1}{2}}$ is transformed to world space to determine $\tilde{q}_{n+1}$ in Equation 14. Finally, the unit Quaternion q_{n+1} and $\boldsymbol{\omega}^b_{n+1}$ are updated. Further details can be found in Zhao and van Wachem[26].

C. Hydrodynamic drag forces and torques on ellipsoidal particles

In this work, the effects of the fluid flow on particles include the hydrodynamic drag force and torque. In general, the drag coefficient strongly depends on particle parameters, such as the particle shape and the particle orientation with respect to the flow, as well as flow conditions such as turbulence level and Reynolds number. For ellipsoidal particles, the following drag force expression derived by Brenner[23] is applied

$$F_i^{drag} = \mu^f \pi a K_{ij}(u_j^{f@p} - u_j^p) \tag{17}$$

where μ^f is fluid dynamic viscosity, $\boldsymbol{u}^{f@p}$ represents the undisturbed fluid velocity at the center of the particle, and $\overline{\overline{K}}$ is the resistance tensor, strongly depending on the orientation of the particle in world space. Using Equation 12, $\overline{\overline{K}}$ can be simply transformed as:

$$\overline{\overline{K}} = (q(q\overline{\overline{K}}^b q^{-1})^T q^{-1})^T \tag{18}$$

Here, $\overline{\overline{K}}^b$ is a constant resistant tensor in body space and determined by the aspect ratio, λ, of the ellipsoidal particle. The off-diagonal components of it are zero, whereas three diagonal

components are defined by

$$K^b_{xx} = \frac{8(\lambda^2-1)^{3/2}}{\left[(2\lambda^2-1)\ln(\lambda+\sqrt{\lambda^2-1}) - \lambda(\sqrt{\lambda^2-1})\right]} \tag{19}$$

$$K^b_{yy} = K^b_{zz} = \frac{16(\lambda^2-1)^{3/2}}{\left[(2\lambda^2-3)\ln(\lambda+\sqrt{\lambda^2-1}) + \lambda(\sqrt{\lambda^2-1})\right]} \tag{20}$$

For approximating the hydrodynamic torque, $\boldsymbol{T}_i^{b,h}$, on an ellipsoid in body space, Jeffery's equation[21] is used, given as,

$$T^{b,h}_x = \frac{32\pi\mu^f a^3\lambda}{3(\alpha_2+\alpha_3)}(\Omega^{bf}_{zy} - \omega^{bp}_x) \tag{21}$$

$$T^{b,h}_y = \frac{16\pi\mu^f a^3\lambda}{3(\alpha_3+\lambda^2\alpha_1)}\left[(1-\lambda^2)S^{bf}_{xz} + (1+\lambda^2)(\Omega^{bf}_{xz} - \omega^{bp}_y)\right] \tag{22}$$

$$T^{b,h}_z = \frac{16\pi\mu^f a^3\lambda}{3(\alpha_2+\lambda^2\alpha_1)}\left[(\lambda^2-1)S^{bf}_{yx} + (1+\lambda^2)(\overline{\overline{\Omega}}^{bf}_{yx} - \omega^{bp}_z)\right] \tag{23}$$

where three constants α_1, α_2 and α_3 are[24],

$$\alpha_1 = -\frac{2}{\lambda^2-1} - \frac{\lambda}{(\lambda^2-1)^{3/2}}\ln\left[\frac{\lambda-(\lambda^2-1)^{1/2}}{\lambda+(\lambda^2-1)^{1/2}}\right] \tag{24}$$

$$\alpha_2 = \alpha_3 = \frac{2}{\lambda^2-1} + \frac{\lambda}{2(\lambda^2-1)^{3/2}}\ln\left[\frac{\lambda-(\lambda^2-1)^{1/2}}{\lambda+(\lambda^2-1)^{1/2}}\right] \tag{25}$$

and the fluid strain rate tensor $\overline{\overline{S}}^{bf}$ and the rotation tensor $\overline{\overline{\Omega}}^{bf}$ are expressed as:

$$S^{bf}_{ij} = \frac{1}{2}\left(\frac{\partial u^{bf}_i}{\partial x_j} + \frac{\partial u^{bf}_j}{\partial x_i}\right) \tag{26}$$

$$\Omega^{bf}_{ij} = \frac{1}{2}\left(\frac{\partial u^{bf}_i}{\partial x_j} - \frac{\partial u^{bf}_j}{\partial x_i}\right) \tag{27}$$

All the fluid velocity derivatives, $\partial u^{bf}_i/\partial x_j$, are evaluated in the particle framework (body space).

It should be noted that the above approach is limited to low particle Reynolds and low particle rotational Reynolds number.

D. Particle coupling with the fluid flow

The above hydrodynamic effects can also inversely influence the channel flow. The rotational Stokes numbers of interest are assumed to be small, so that the effect of hydrodynamic torques can be neglected, an assumption consistent with the fact our particles are assumed

to be much smaller than a mesh cell. Only the effect of the particle drag force is adopted as the source term Π_i in the Navier-Stokes Equation 2,

$$\Pi_i = -\frac{1}{V_{cell}^f} \sum_{l=1}^{N_p} F_i^{drag,l} \tag{28}$$

where N_p is the number of particles in a fluid computational cell, V_{cell}^f is the volume of a fluid cell, and drag forces, F_{drag}, are summed in the cell and volume averaged. This approach is referred to as the particle-source-in-cell method, and requires an interpolation scheme to transform the properties between Lagrangian properties and the Eulerian fluid cell. The cubic spline scheme proposed by Yeung and Pope[35] is applied in this work.

E. Inter-particle and particle-wall collision force and torque

In earlier studies[9,10,12], both particle-particle and particle-wall collisions were neglected by the dilute flow condition. However, it is not precisely clear at what mass loading and particle volume fraction particle collisions become important for non-spherical ellipsoids. Furthermore, the behaviour of ellipsoids is more complex than spheres after collision. Therefore, particle collisions are detected in this study, and their contribution is then added in the overall forces and torques on the particles. For this purpose, this paper applies a realistic deterministic collision model, the soft-sphere collision model.

To appropriately detect all contact points of collisions, each ellipsoid is constructed of a large number of small, fictitious spheres, and the hull of all fictitious spheres in an ellipsoid provide an accurate representation of the ellipsoid surface. A collision is detected when two fictitious spheres from different non-spherical particles overlap. When a particle collision occurs, the soft-sphere model determines a slight overlap at the contact point. And this overlap is then used to approximate the local deformation of the colliding particle, and the corresponding normal and tangential forces applied at the point of the contact. These forces are determined by using the Hertzian-Mindlin force model derived by Mindlin and Deresiewicz[36]

$$\begin{aligned} \boldsymbol{F}_n(t) &= K_n(t)\delta_n^{\frac{3}{2}}(t)\boldsymbol{n}(t) \\ \boldsymbol{F}_t(t) &= \min\left(\mu \boldsymbol{F}_n(t), K_t(t)\boldsymbol{\delta}_t(t)\right) \end{aligned} \tag{29}$$

where μ is the coefficient of friction, $\delta_n(t)$ is the normal displacement scalar, and $\boldsymbol{\delta}_t(t)$ represents the the total tangential displacement vector, which is derived by integrating the

successive tangential displacements and mapping this into the current reference framework of the collision. In Equation 29, K_n and K_t are the spring constants for the normal and tangential forces, respectively, as predicted by Hertzian contact theory,

$$K_{n,l}(t) = \frac{4}{3}E^*\sqrt{r(t)}$$
$$K_t(t) = 8G^*\sqrt{r(t)\delta(t)}$$

where $r(t)$ represents the local radius of the particle-particle contact area, E^* is the normal spring constant, G^* is the tangential constants and the subscript l represents loading, *i.e.* the particles moving towards each other. To account for the dissipative nature of particle-particle and particle-wall collisions, a coefficient of restitution $e = \sqrt{K_{n,u}/K_{n,l}}$ is applied, determining the spring constant value for unloading, represented by the subscript u.
The subsequent forces and torques of the particle-particle and particle-wall collisions are then added to both of the particles in contact. The collisional torque for each collision is determined by

$$\boldsymbol{T}^c = (\boldsymbol{F}_n + \boldsymbol{F}_t) \times \boldsymbol{X}_{mp-cp} \tag{30}$$

where $\boldsymbol{X}_{mp-cp}$ represents the vector from the center of the particle to the contact point of the collision. Note that the above equation is expressed in world-space and is converted to body space for the application in Equation 5.

III. SIMULATION SET-UP

All simulations of gas-solid channel flow are carried out in our in-house flow solver[37]

A. Fluid properties and computational domain

Table I lists the properties of the fluid flow. The fluid response time (τ_f) and friction length scale (l_τ) are determined based on the viscosity (ν^f) and friction velocity (u_τ). All results are plotted and analyzed by scaling with these wall units, and so denoted with the superscript $+$.
As shown in Table II, the computational channel domain with two smooth walls is $4\pi h \times 2h \times 2\pi h$ large in stream-wise (x), wall-normal (y) and span-wise (z) directions, respectively.

Parameter	Definition	Value(Units)
ρ^f		1.3 (kg/m^3)
ν^f		1.57×10^{-5} (m^2/s)
u_τ	$u_\tau = \sqrt{\tau_0/\rho^f}$	0.11775 (m/s)
l_τ	$l_\tau = \nu^f/u_\tau$	1.333×10^{-4} (m)
τ_f	$\tau_f = \nu^f/u_\tau^2$	0.001132 (s)
Re_τ	$Re_\tau = u_\tau h/\nu^f$	150 (-)
St^+	$St^+ = \frac{\tau_p}{\tau_f}$	see Table 3
δP_1	$\delta P_1 = \frac{\rho^f {\nu^f}^2 Re_\tau^2}{h^3}$	0.90123 (Pa/m)

TABLE I. The properties of the fluid and the flow

In the wall-normal direction, no-slip boundary conditions are applied at the walls, whereas a periodic boundary is set in the other two directions. The computation is executed on $159 \times 169 \times 159$ grid points. The grid spacing is uniform in the stream-wise and span-wise directions but refined towards the walls in the wall-normal direction by using a tanh distribution with a growth factor of 1.6 on both sides, given for the grid point number n,

$$y_n = y_{max}\left[\frac{1}{2}\left(\frac{1+\tanh\left(1.6*\left(\frac{n*\Delta y}{y_{max}}-\frac{1}{2}\right)\right)}{\tanh\left(\frac{1}{2}*1.6\right)}\right)\right] \tag{31}$$

This refinement ensures there are at least 4 grid points within $y^+ <= 5$ layer of the wall. The spatial resolution is also summarised in Table II. These are comparable to the studies by Kim *et. al.*[38] and Marchioli *et. al.*[6].

In the fluid continuity and momentum equations, the advective terms are approximated by a second order accurate central differencing scheme, while the temporal terms are com-

Directions	Stream-wise (x)	Wall-normal (y)	Span-wise (y)
Length (m)	0.2511 ($2\pi h$)	0.039963 ($2h$)	0.125549(πh)
Number of grid points	159	169	159
Spatial resolution($\triangle x^+$)	11.7	$0.57 \sim 2.18$	5.897

TABLE II. The properties of the computational domain and grid mesh in all three directions

puted with the second order 3 point backward Euler scheme with respect to the time-step. Moreover, the time step (Δt^f) for the fluid phase equals 1×10^{-4} (s), corresponding to non-dimensional form $\Delta t^{f^+} = 0.08826$. These numerical settings ensure the computational accuracy required for DNS.

B. Particle properties

The properties of the particles in all simulations are listed in Table III. Simulations are separated by different *global* Stokes numbers (St^+) and different ellipsoid aspect ratios, λ. The global Stokes number, $St^+ = \tau_p/\tau_f$, is determined by the particle response time τ_p and the *average* or *global* fluid response time τ_f, both defined in Table I.

For ellipsoidal particles, τ_P can be derived directly from the drag force expression, Equation 17, for these particles[23] as has been demonstrated in[39]:

$$\tau_p = \frac{2a^2\rho^p}{9\nu^f\rho^f}\frac{\lambda\ln(\lambda+(\lambda^2-1)^{\frac{1}{2}})}{(\lambda^2-1)^{\frac{1}{2}}} \tag{32}$$

where a and λ are the length of semi-minor axis and aspect ratio of the ellipsoid. The particle response time for a spherical particle can be expressed as[28]:

$$\tau_p = \frac{\rho^p D_p^2}{18\mu^f} \tag{33}$$

where D_p is the sphere diameter. This is indeed the limit of Equation 32 for $\lambda \to 1$.
If the semi-minor axis, a, is kept constant, the drag force for an ellipsoid, expressed by

St^+	λ	ρ $[kg/m^3]$	minor-axis $(a)[\mu m]$	Major-axis (b) $[\mu m]$	numbers (N)	Volume fraction [%]
5.0	1.0	225.68	96.0	96.0	200,000	0.0073
30	1.0	1354.21	96.0	96.0	200,000	0.0073
5.0	3.0	120.77	96.0	287.93	200,000	0.022
30.0	3.0	724.23	96.0	287.93	200,000	0.022
5.0	5.0	93.7	96.0	480.0	200,000	0.036
30.0	5.0	578.77	96.0	480.0	200,000	0.036

TABLE III. The properties of the particles used in the simulations

Equation 17, increases as the aspect ratio of the ellipsoid increases. In order to isolate the effects of particle shape alone, the effective drag has been kept the same as for spherical particles, by adjusting the density; *i.e.*, the ellipsoidal particles have a lower value of density to precisely compensate. These values for density are provided in Table III. The result is that the global Stokes number and dimensionless drag characteristics are approximately the same as for the corresponding heavier spheres.

The simulations are initialized with the results from single phase flow simulations. After single phase fluid channel flow reach steady-state, particles are homogeneously positioned in the whole channel with a velocity of the bulk fluid velocity without rotation in each case. In order to ensure the accuracy of the soft-sphere collision model for the given particles and flow conditions, the particle time-step Δt^p is chosen to be very small, 1×10^{-7}. This time-step is 1000 times smaller than the fluid time step. To avoid any energy loss during particle collisions, the restitution coefficient e equals one. A velocity-Verlet temporal discretization is employed for the particle translational motion equations, while the PCDM algorithm is

applied for the rotation of ellipsoidal particles.

IV. MODELLING RESULTS AND DISCUSSION

The present work focuses on exploring the effects of the particle shape and global Stokes numbers on both fluid and particle phases. In gas-solid multiphase flows, there are several factors contributing to the fluid flow modulation, such as the particle size, the particle volume fraction, Reynolds number, the wall roughness, global Stokes number and the particle shape. In this study, particles are considered as point-particles for the fluid phase, and all simulations contain the same number of particles, *i.e.* 200,000. The friction Reynolds number is fixed at 150 by keeping the pressure drop in the stream-wise over the channel constant. Additionally, smooth wall conditions are applied. The differences in the particle size, friction Reynolds number and wall roughness are negligible in all simulations, but the other two factors, *i.e.* the global Stokes number, St^+, and the particle shape are varied. Therefore, the effects of particle shapes and global Stokes numbers on both particle and fluid phases can be well studied.

A. Fluid Statistics

In this section, fluid statistics are displayed and analysed, including the fluid velocity, all terms in the turbulence kinetic energy (TKE) equation, the major components of the fluid flow dissipation rate and the mean square vorticity.

1. Fluid velocity statistics

Figs. 2 to 9 compare the mean fluid velocity U_1^{f+} in the flow direction, the fluid root mean square (RMS) velocity $u_i'^{f+}$ and Reynolds stresses $< u_x'^{f+} u_y'^{f+} >$ among all 6 particle-laden simulations and the single phase flow simulation. For the RMS (root mean square) values of variables, the superscript prime is used, while capital letters represent mean values of the variables. The symbols <> represent the averaging operator.

Fig. 2 displays the mean fluid flow velocities U_1^{f+} from the wall, $y^+ = 0$, to the channel center, $y^+ = 150$. The curves of the mean fluid flow velocities in all particle-laden simulations nearly coincide in the very near wall region ($0 < y^+ < 10$) as shown in Fig. 3. *This collapse in*

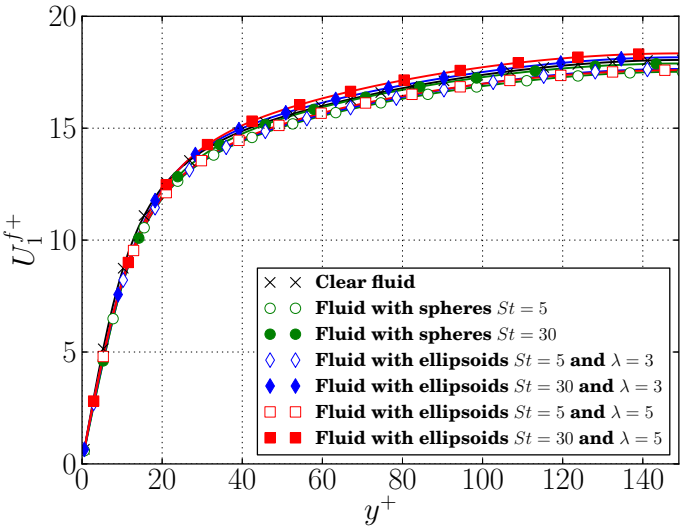

FIG. 2. Fluid mean velocity in the flow direction as a function of distance to the wall

classic inner variables together with the constancy of the wall shear stress means that the viscosity of the flow with particles must be the same as for the flow without. As can be seen in Figs. 2 and 4, there is an increase in U_1^f between $40 < y^+ < 150$ for the cases with large global Stokes number ($St^+ = 30$). This will be seen to be because particles with high inertia

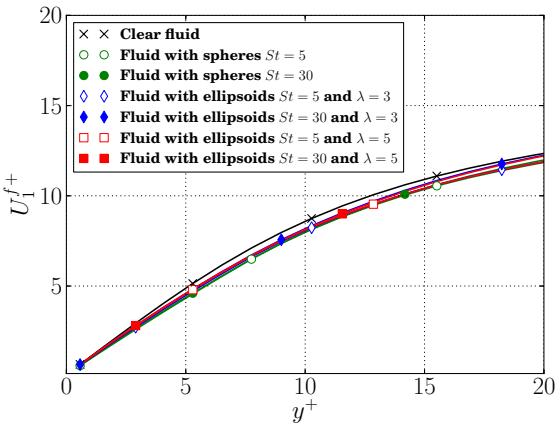

FIG. 3. Fluid mean velocity in the flow direction as a function of distance to the wall in the near wall region

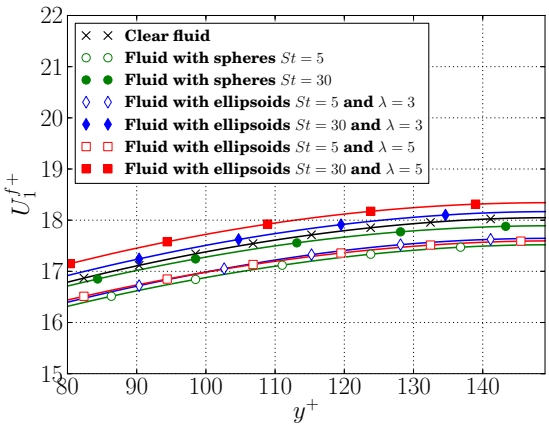

FIG. 4. Fluid mean velocity in the flow direction in the central region of the channel

attenuate the turbulence intensity and cause a drag reduction in the channel flow. The mean fluid velocity in the cases with high particle inertia ($St^+ = 30$) is larger in the outer

region ($40 < y^+ < 150$), compared to the cases with relatively low St^+ ($St^+ = 5$), even in such dilute flows. The bulk fluid velocity increases from 1.750 m/s in the case considering spheres with $St^+ = 5$ to 1.832 m/s in ellipsoid-laden case with $\lambda = 5$ and $St^+ = 30$. It is also clearly observed from Fig. 4 that U_1^{f+} in the cases considering particles of $St^+ = 30$ increases with increasing particle aspect ratio in the channel central region. The elongated shape of ellipsoids with considerably high inertia clearly strengthens the effect of particles on the fluid flow and enhances the drag reduction, thus increasing the mean flow velocity. Moreover, since the profile of U_1^{f+} collapses perfectly near $y = 0$ and u_τ is constant and has the same value for all simulations, this means that the viscosity ν^f is equal in all cases. Therefore, the drag reduction has nothing to do with changes in the viscosity due to the particles. This also implies that the changes in the flow due to the presence of particles has everything to do with the turbulence.

It is generally believed that in gas-solid channel flow, dispersed small particles with high particle inertia increase the fluid stream-wise RMS velocity, but reduce velocity fluctuations in the other two directions[13]. These phenomena seem to be caused by two factors: the inertia of particles and the flow velocity gradients. In the wall-normal and span-wise directions, particles with high inertia cannot respond quickly to changes of the fluid flow and delay it, resulting in the decrease of the fluid RMS velocities in these two directions. As can be seen

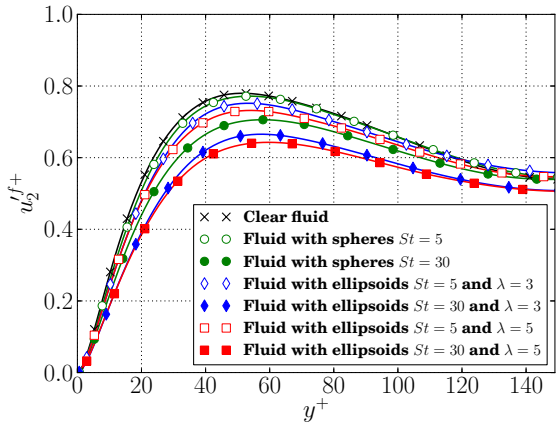

FIG. 5. Fluid RMS velocity in the wall-normal direction as a function of distance to the wall

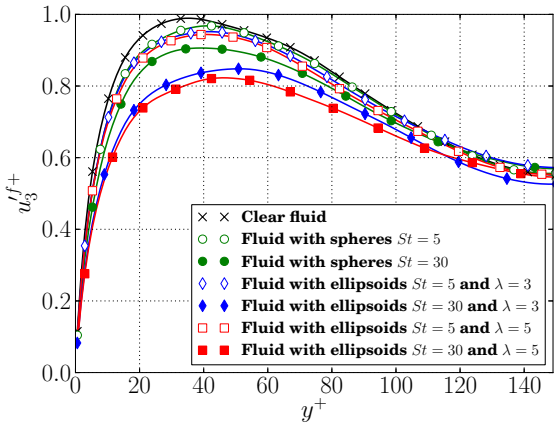

FIG. 6. Fluid RMS velocity in the span-wise direction as a function of distance to the wall

in Figs. 5 and 6, the velocity fluctuations in the wall-normal and span-wise directions in all particle-laden cases are smaller than for the clear fluid flow, especially within the region

($0 < y^+ < 80$). The higher the particle inertia, the lower the fluid RMS velocities in the wall-normal and span-wise directions. It is also clearly observed from Figs. 5 and 6 that the effect of the elongated shape further decreases the fluid velocity fluctuations in these two directions in the cases with the same Stokes number. This is because the interactions between ellipsoidal particles and the fluid flow strongly depend on the particle orientation and are more complex and stronger than those between spheres and the fluid. Thus the effect of elongated shape further decreases the fluid velocity fluctuations in the wall-normal and span-wise directions in the cases with the same Stokes number. Because the mean fluid velocities in these two direction are zero throughout the channel, their gradients are also close to zero, and so there is, of course, no effect of the fluid velocity gradient on the fluid velocity fluctuations in the wall-normal and span-wise directions. In addition, the peaks of $u_2'^{f+}$ and $u_3'^{f+}$ shift towards the center of the channel as particles get heavier.

The situation is more complex in the stream-wise direction. Like the other directions, the fluid velocity fluctuation in the stream-wise direction is somewhat reduced by particles with high inertia. Due to no-slip conditions applied at the walls for the fluid phase and the non-zero mean stream-wise velocity, the continuous fluid flow has a large velocity gradient in the near wall region. When the particles with high inertia move vertically in the wall-normal direction, the large momentum transfer between the two phases strengthens the velocity fluctuations of both the particles and the fluid flow. As the Stokes number rises, the velocity profiles of particles in the stream-wise direction becomes flatter. This considerably enlarges the slip velocity and strengthens momentum transfer between the fluid flow and particles. Fig. 7 shows the fluid RMS velocity $u_1'^{f+}$ in the stream-wise direction. In the particle-laden cases with relatively low Stokes number ($St^+ = 5$), the peaks of $u_1'^{f+}$ are slightly higher than in clear fluid flow case, and the effect of increasing particle aspect ratio is not clearly observed. In the cases with large Stokes number ($St^+ = 30$), the effect of the velocity gradient is dominant, and $u_1'^{f+}$ therefore increases significantly between $15 < y^+ < 150$. Moreover, $u_1'^{f+}$ further rises with increasing particle aspect ratio in these cases with $St^+ = 30$. Thus the elongated shape of ellipsoids with high inertia can considerably strengthen the fluid-particle interactions and enhance the effect of the velocity gradient on the fluid RMS velocity in the stream-wise direction. As can be seen in Fig. 8, it is important to note that the large effects notwithstanding away from the wall, all profiles of $u_1'^{f+}$ collapse in classic inner variables very close to the wall ($y^+ < 5$). This is consistent with the observation above that the

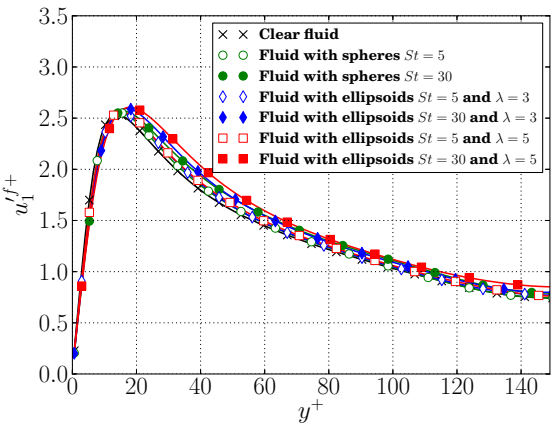

FIG. 7. Fluid RMS velocity in the stream-wise direction as a function of distance to the wall

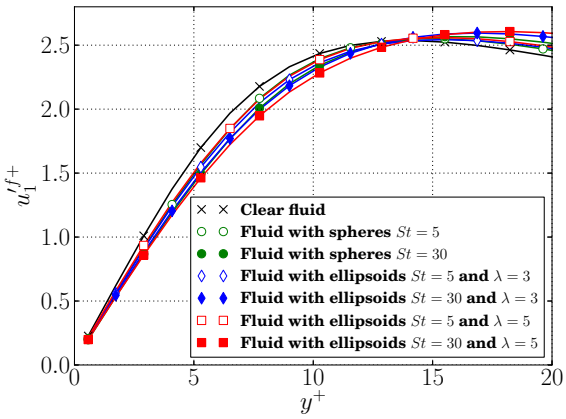

FIG. 8. Fluid RMS velocity in the stream-wise direction as a function of distance to the wall

particles have at most a very minimal effect on the fluid viscosity, as might be expected in view of their very dilute concentrations. Obviously, the reasons for the changes at larger distances from the wall must lie elsewhere.

Fig. 9 shows that the magnitude of the Reynolds stress decreases with increasing particle aspect ratio and Stokes number. The reduction of the Reynolds stress confirms that the

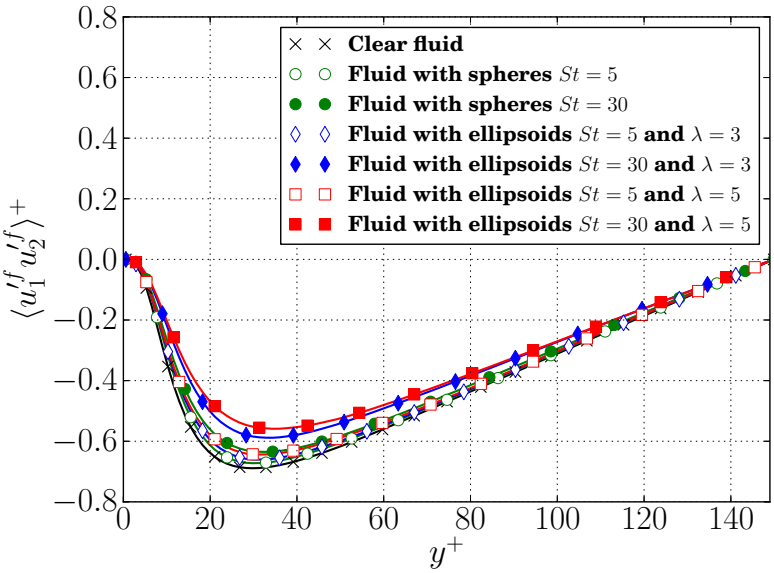

FIG. 9. Reynolds stress as a function of distance to the walls

flow turbulence is attenuated in the cases with large Stokes number, even in dilute flow conditions, and the elongated shape of non-spherical ellipsoids tends to further strengthen

the turbulence modification. It should be also noted that the position of the minimum Reynolds stresses slightly shift towards the center of the channel as well as the peak points of fluid RMS velocities in the particle-laden cases.

2. Turbulence Kinetic energy (TKE) equation

To explore how dispersed particles influence the turbulence, the TKE equation is discussed here. For a fully developed gas-solid channel flow, the TKE equation can be simplified into

$$\frac{d}{dy}\left(\frac{1}{2} < u_y'^f u_i'^f u_i'^f > + \frac{< u_y'^f p' >}{\rho^f} - \nu^f \frac{d}{dy}(k + < u_y'^{f2} >)\right) = \mathcal{P} - \tilde{\varepsilon} - \varepsilon_p \tag{34}$$

where k is the turbulent kinetic energy, $\mathcal{P}$ is the production of turbulence, $\tilde{\varepsilon}$ is the fluid flow dissipation rate, and ε_p represents the dissipation caused by the coupling with particles. The three terms in the bracket on the left hand side of the equation are the turbulence transport: by the turbulence itself, by the pressure fluctuations and by the viscous stresses, respectively. The production, $\mathcal{P}$, is defined by

$$\mathcal{P} = - < u_x'^f u_y'^f > \frac{dU_x^f}{dy} \tag{35}$$

and $\tilde{\varepsilon}$ is given as:

$$\tilde{\varepsilon} = 2\nu^f < s_{ij}'^f s_{ij}'^f > \tag{36}$$

The dissipation rate caused by the work done by the coupling from particles, ε_p, can be directly derived from the source term Π_i in Equation 2 as:

$$\varepsilon_p = - < \Pi_i' u_i'^f > \tag{37}$$

3. Turbulence transport terms

On the left hand side of Equation 34, the three transport terms (turbulence kinetic energy flux due to turbulence itself, the pressure fluctuations and viscous stresses) only transport the TKE from one location to another, but do not generate any TKE. Figs. 10 to 12 show these turbulence transport terms between $0 < y^+ < 60$. As shown in Fig. 12, the viscous transport term peaks at the wall and transports a large amount of TKE to the wall. This is consistent with the largest value of the fluid dissipation rate at the wall, where the other three terms in Equation 34 are all close to zero. The peak and minimum values of all three

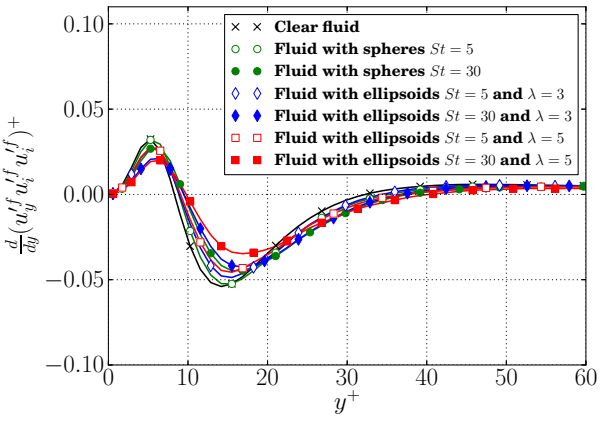

FIG. 10. TKE turbulence itself transport term as a function of distance to the wall

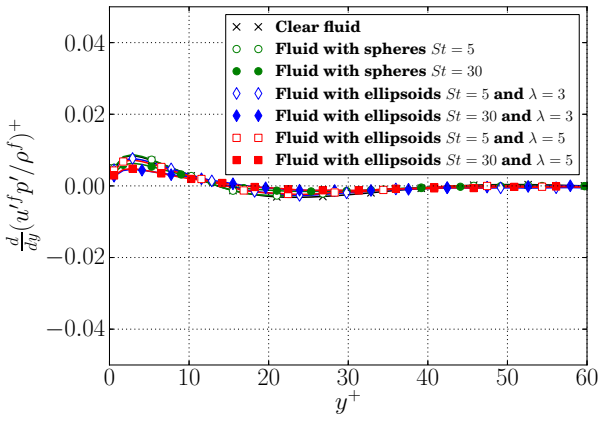

FIG. 11. TKE pressure fluctuation transport term as a function of distance to the wall

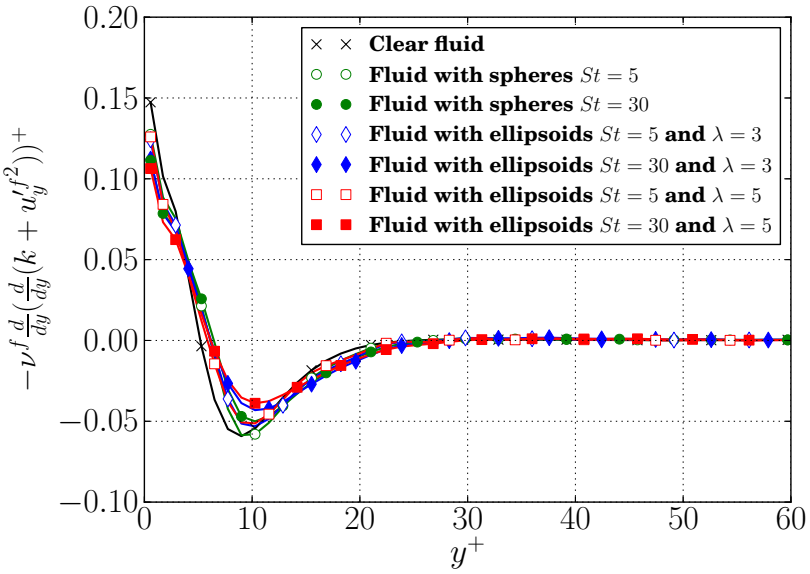

FIG. 12. TKE viscous transport term as a function of distance to the wall

terms near the wall are slightly reduced, with the particles of increasing Stokes number and aspect ratio. In the region far away from the wall, $40 < y^+ < 150$, the pressure fluctuations and viscous transport terms in all simulations are almost zero, while the turbulence itself transport term is slightly larger than zero, around 0.005. These results indicate that the turbulence transport is weak in the central region of the channel. Finally, note that like all the preceding plots, the region closest to the wall collapses in classic wall variables using the fluid viscosity which is the same for all simulations. So clearly the effects on the turbulence

cannot be related to a viscosity change.

4. *The production of turbulence*

Fig. 13 shows that the dimensionless turbulence production $\mathcal{P}^+$ rises steeply from 0 at the wall to a peak value around $y^+ \approx 11$ to 15, and then smoothly drops to 0 again towards the center of the channel. Like the preceding plots, the region very close to the wall ($y^+ < 5$) collapses in inner variables, consistent with the observations above that the kinematic viscosity is unaffected by the particles. As the Stokes number rises, the peak value

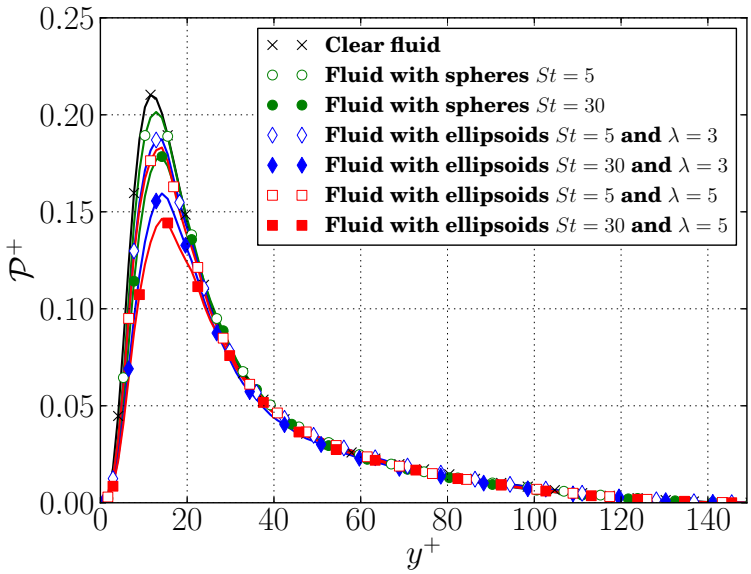

FIG. 13. The production of turbulence as a function of distance to the wall

of $\mathcal{P}^+$ decreases from 0.2096 for the single phase case to 0.1455 for the ellipsoid-laden case with $\lambda = 5$ and $St = 30$. This shows that particles with high inertia reduce the turbulence production of the fluid flow. Similar to the velocity statistics, the peaks of the production slightly move towards the center of the channel. Furthermore, particles with large aspect ratio show lower values of $\mathcal{P}^+$ compared to particles with a smaller aspect ratio and the same global Stokes number.

5. *Dissipation terms*

The minus fluid turbulence dissipation rate ($-\tilde{\varepsilon}^+$) is plotted in Fig. 14, in which $-\tilde{\varepsilon}^+$

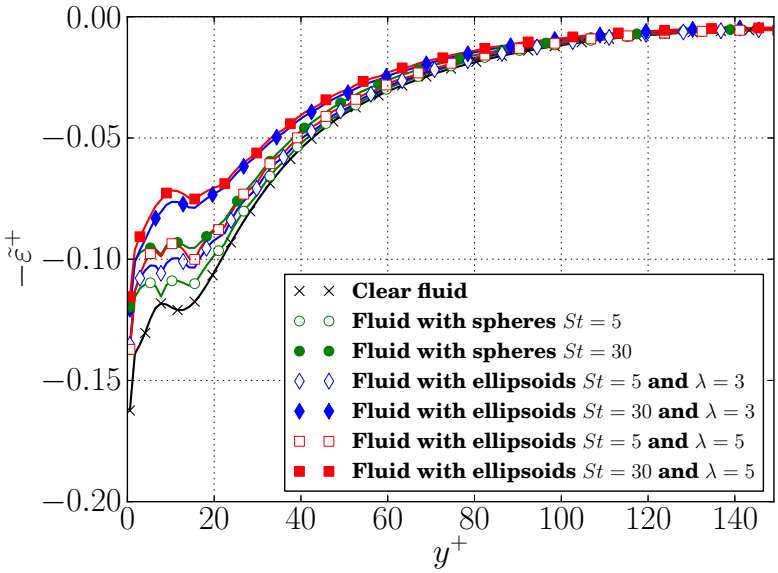

FIG. 14. The minus fluid flow dissipation rate as a function of distance to the wall

has the largest magnitude at the wall and decreases towards the central region. In the near wall region, it is clearly observed that increasing Stokes number and particle aspect ratio contributes to an increase in the fluid dissipation rate. In addition, $-\tilde{\varepsilon}^+$ in all particle-laden cases tends to smoothly rise between $60 < y^+ < 150$ and reach almost the same small absolute value at the center of the channel. This behaviour very near the wall is quite remarkable, and nothing like the previous plots. It does not make sense that viscosity would be one thing for the dissipation, and something quite different for everything else. So clearly the effect of the particles is either to dissipate the energy directly by its interaction with the fluid by means of drag and lift (to make up the difference), or to change the turbulence flow structures doing the dissipation. It will be seen in the next paragraph that the particle dissipation is itself nearly insignificant. So the differences observed here must be directly related to changes in flow structures.

Fig. 15 shows the minus dissipation rate caused by the coupling force of the particles, $-\varepsilon_p^+$. In Equation 37, $-\varepsilon_p^+$ is the value of the covariance of the particle-fluid interaction force fluctuations and fluid velocity fluctuations and is influenced by two factors: the local particle volume fraction and the slip velocity between the particles and the fluid. As the particles preferentially accumulate in the near wall region, $-\varepsilon_p^+$ peaks near the wall as shown in Fig. 15. The magnitude of ε_p^+ is orders of magnitude smaller, compared to the fluid

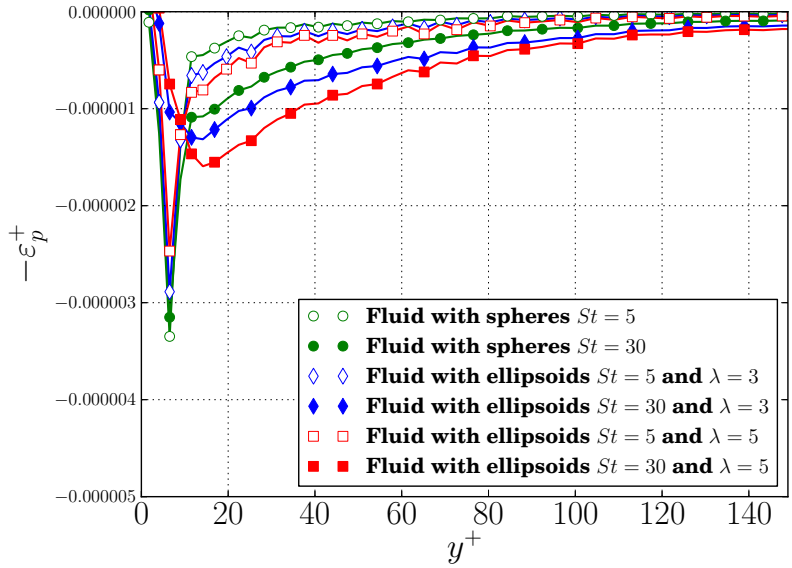

FIG. 15. The dissipation rate caused by the coupling force from particles as a function of distance to the wall

flow dissipation rate $\tilde{\varepsilon^+}$, and thus the contribution of ε_p^+ to dissipate the flow turbulence is negligible. Therefore, the significant effect on the flow turbulence due to the two-way coupling between particles and the fluid flow is not directly attributable to the increased dissipation by the particles, *i.e.* ε_p. Nonetheless, two-way coupling must be taken into account, since it has a dramatic effect on both the dissipative structures very near the wall, as well as those producing the turbulence kinetic energy near the peak in productions.

6. Components of the fluid flow turbulence dissipation

In view of the large effects on the near wall dissipation it is useful to examine whether and how the components of the dissipation and vorticity are affected by the particles. The expression for the fluid dissipation rate contains a total of twelve components (nine mean square derivative terms and three cross terms) given as

$$\begin{aligned}\tilde{\varepsilon} =&\nu[2(<{u'^f_{1,1}}^2>+<{u'^f_{2,2}}^2>+<{u'^f_{3,3}}^2>)\\ &+(<{u'^f_{1,2}}^2>+<{u'^f_{2,1}}^2>+<{u'^f_{1,3}}^2>+<{u'^f_{3,1}}^2>+<{u'^f_{3,2}}^2>+<{u'^f_{2,3}}^2>)\\ &+2(<u'^f_{1,2}u'^f_{2,1}>+<u'^f_{1,3}u'^f_{3,1}>+<u'^f_{2,3}u'^f_{3,2}>)]\end{aligned} \tag{38}$$

Only three components, $< u_{1,2}'^{f\ 2} >$, $< u_{3,2}'^{f\ 2} >$ and $< u_{1,3}'^{f\ 2} >$, significantly contribute to $\tilde{\varepsilon}$, whereas the other nine components are much smaller than these three. Figs. 16 to 18 show the three main components in the fluid dissipation rate for the various cases. Strikingly different from all the plots above are the dramatic effects very close to the wall, especially for $< u_{1,2}'^{f+2} >$ and $< u_{3,2}'^{f+2} >$, which do not collapse in classical viscous variables. The effects over the rest of the flow mirror those of the dissipation as a whole and the production, with large effects near the kinetic energy peak near $y^+ = 11$. These can only be explained by a change in turbulence structure due to the presence of particles. In Figs. 16 and 18,

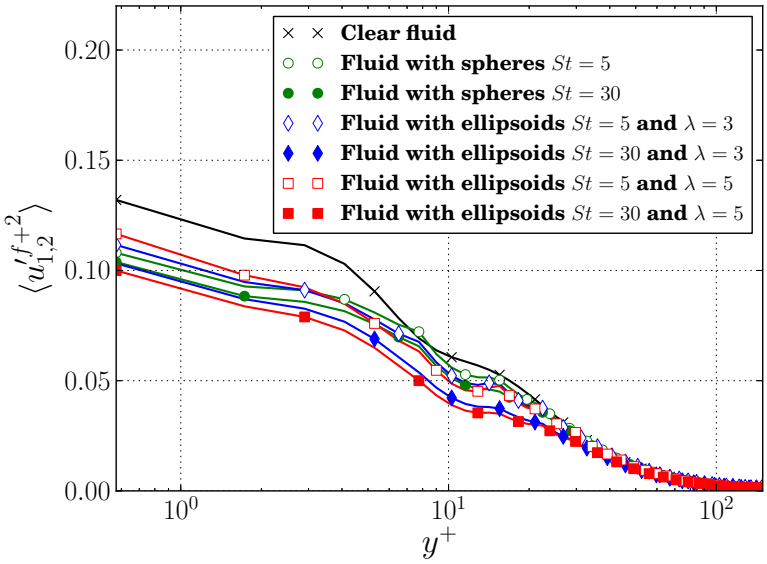

FIG. 16. Mean-square derivative $< u_{1,2}'^{f+2} >$ as a function of distance to the wall

both $< u_{1,2}'^{f+2} >$ and $< u_{3,2}'^{f+2} >$ decrease within $y^+ < 5$ when particles are added to the flow. The combination of these reductions results in a decrease in the magnitude of $\tilde{\varepsilon}$ the linear sublayer, as can be seen from Fig. 14. The local peak and minimum values of $\tilde{\varepsilon}$ in buffer layer are obviously caused by the rise in $< u_{1,3}'^{f+2} >$ and $< u_{3,2}'^{f+2} >$ in the region of $5 < y^+ < 15$. Around $y^+ = 10$, the deflection of $< u_{1,2}'^{f\ 2} >$ and the peak of $< u_{1,3}'^{f+2} >$ are results of the "low-speed" streaks in the near wall region. For particle-laden cases, all the components of the fluid turbulence dissipation decrease as the particle inertia and aspect ratio increase in the near wall region, but these effects are not important in the region between $80 < y^+ < 150$.

In the literature, the fluid flow dissipation rate, the mean square vorticity and their compo-

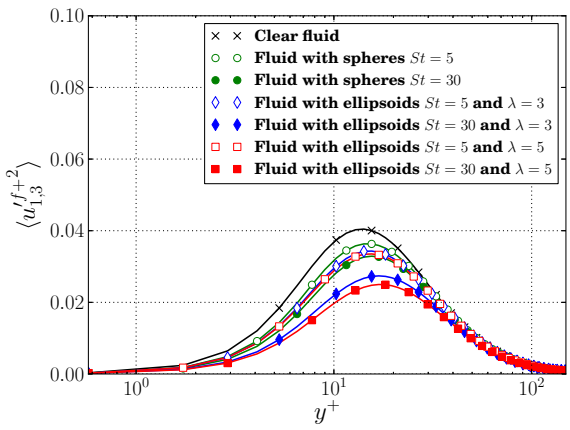

FIG. 17. Mean-square derivative $< u_{1,3}'^{f+2} >$ as a function of distance to the wall

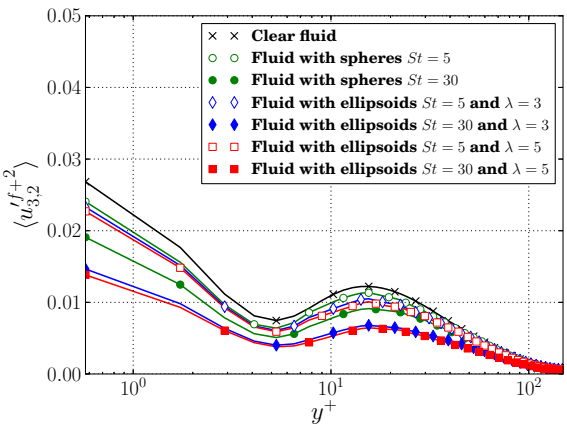

FIG. 18. Mean-square derivative $< u_{3,2}'^{f+2} >$ as a function of distance to the wall

nents are widely reported for a single phase fluid channel flow[38,40–43], and the assumption of local isotropy and local axisymmetric turbulence in the channel center were also discussed. This study explores these assumption for the gas-solid turbulent flow.

The isotropic dissipation rate of the fluid, $\tilde{\varepsilon}_{iso}$, is defined by a square derivative term,

$$\tilde{\varepsilon}_{iso} = 15\nu^f < u_{1,1}'^{f\ 2} > \tag{39}$$

or,

$$\tilde{\varepsilon}_{iso} = \frac{15}{2}\nu^f < u_{1,2}'^{f\ 2} > \tag{40}$$

and the fluid homogeneous dissipation rate $\tilde{\varepsilon}_{hom}$ can be expressed as

$$\tilde{\varepsilon}_{hom} = \nu^f < u_{i,j}'^f u_{i,j}'^f > \tag{41}$$

$\tilde{\varepsilon}_{hom}$ does not contain the three cross-terms, which are cancelled out by less $< u_{1,1}'^{f\ 2} > + < u_{2,2}'^{f\ 2} > + < u_{3,3}'^{f\ 2} >$.

The local axisymmetric turbulence for single phase flow is reported and discussed in earlier studies[38,42]. If it is assumed that the axis of local symmetry is the stream-wise direction, two of many axisymmetric dissipation rates are given as:

$$\tilde{\varepsilon}_{axis_1} = \nu^f \left[\frac{5}{3} < u_{1,1}'^{f\ 2} > +2 < u_{1,3}'^{f\ 2} > +2 < u_{2,1}'^{f\ 2} > + < u_{2,3}'^{f\ 2} > \right] \tag{42}$$

$$\tilde{\varepsilon}_{axis_2} = \nu^f \left[- < u_{1,1}'^{f\ 2} > +2 < u_{1,2}'^{f\ 2} > +2 < u_{2,1}'^{f\ 2} > +8 < u_{2,2}'^{f\ 2} > \right] \tag{43}$$

For all the particle-laden cases, the ratios of $\tilde{\varepsilon}_{iso}$, $\tilde{\varepsilon}_{hom}$, $\tilde{\varepsilon}_{axis_1}$ and $\tilde{\varepsilon}_{axis_2}$ to $\tilde{\varepsilon}$, are in good agreement with the results obtained from the clear fluid case. It seems that dispersed particles do not change the relationship between these modelled dissipation rates and the original dissipation rate at the studied concentrations. This is probably due to the fact that the high particle inertia and elongated shape have almost the same effects on each component of $\tilde{\varepsilon}$ throughout the channel.

7. Vorticity

The flow mean square vorticity $\boldsymbol{\omega}^f$ is defined as the curl of the fluid velocity fluctuation,

$$\omega_i^{f\,2} = \epsilon_{ijk} u'^f_{k,j} \tag{44}$$

where ϵ_{ijk} is the permutation tensor. Three components are separately defined as:

$$\omega_1^{f\,2} = < u'^f_{3,2}{}^2 > + < u'^f_{2,3}{}^2 > -2 < u'^f_{2,3} u'^f_{3,2} > \tag{45}$$

$$\omega_2^{f\,2} = < u'^f_{1,3}{}^2 > + < u'^f_{3,1}{}^2 > -2 < u'^f_{1,3} u'^f_{3,1} > \tag{46}$$

$$\omega_3^{f\,2} = < u'^f_{1,2}{}^2 > + < u'^f_{2,1}{}^2 > -2 < u'^f_{1,2} u'^f_{2,1} > \tag{47}$$

The mean square vorticity can be determined by

$$\begin{aligned} \omega^{f\,2} =& (< u'^f_{1,2}{}^2 > + < u'^f_{2,1}{}^2 > + < u'^f_{1,3}{}^2 > + < u'^f_{3,1}{}^2 > + < u'^f_{3,2}{}^2 > + < u'^f_{2,3}{}^2 >) \\ & - 2(< u'^f_{1,2} u'^f_{2,1} > + < u'^f_{1,3} u'^f_{3,1} > + < u'^f_{2,3} u'^f_{3,2} >) \end{aligned} \tag{48}$$

Similar to the fluid dissipation rate $\tilde{\varepsilon}$, only three components $< u'^f_{1,2}{}^2 >$, $< u'^f_{3,2}{}^2 >$ and $< u'^f_{1,3}{}^2 >$ are dominant in the vorticity.

The results show that the vorticity components $\omega_1^{f\,2}$, $\omega_2^{f\,2}$ and $\omega_3^{f\,2}$ are similar to $< u'^f_{3,2}{}^2 >$, $< u'^f_{1,3}{}^2 >$ and $< u'^f_{1,2}{}^2 >$ respectively, but slightly larger than these mean-square velocity derivatives. This is due to the negative contribution of the cross-terms to $\omega^{f\,2}_i$. The effects of particle inertia and aspect ratio on the vorticity are also as the same as these effects on the three main dissipation rate components. In the near wall region of $0 < y^+ < 30$, each vorticity component in the particle-laden cases decreases with the increasing particle inertia and aspect ratio.

B. Contour plots of instantaneous fluid velocities

Figs. 19 and 20 show the instantaneous fluid velocity with particles in the wall-normal direction (u_2^f) in the cross-sectional y-z plane at $x^+ = 942$ for the case considering spheres with $St^+ = 5$ and the case considering ellipsoids with $St^+ = 30$ and $\lambda = 5$, respectively.

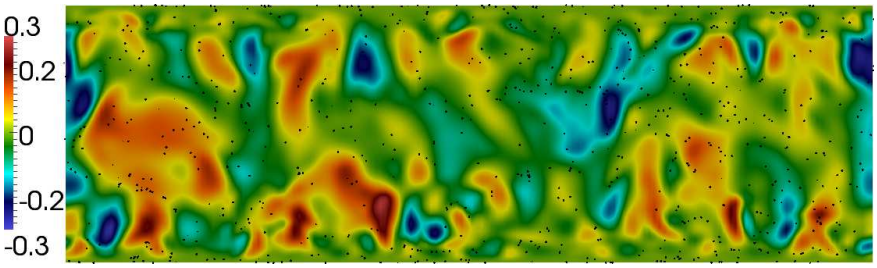

FIG. 19. The instantaneous fluid velocity (indicated by colour) in the wall-normal direction and the distribution of spherical particles with $St^+ = 5$ near the cross-sectional y-z plane at $x^+ = 942$

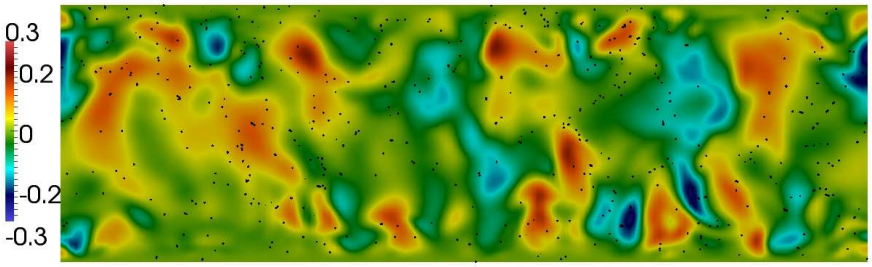

FIG. 20. The instantaneous fluid velocity (indicated by colour) in the wall-normal direction and the distribution of ellipsoids with $St^+ = 30$ and $\lambda = 5$ near the cross-sectional y-z plane at $x^+ = 942$

The black dots represent the small particles around the plane. Comparing these two figures, it is clearly observed that the size and number of the high speed areas (red circle zones) decrease with increasing particle inertia and aspect ratio, and particles spend less time in these high speed areas.

Figs. 21 and 22 show the contour plots of the fluid velocity with particles in the stream-wise direction (u_1^f) in the x-z plane at $y^+ = 8$. In these two figures, the blue regions, *i.e* low fluid velocity areas, represent the low-speed streaks in the channel flow. This feature is clearly seen in both cases with spheres and ellipsoids. As particle inertia and aspect ratio rises, the low-speed streaks become wider and more distinct. Between the low-speed streaks, the fluid moves relatively faster (dark red zones). In the near wall region of a turbulent channel flow,

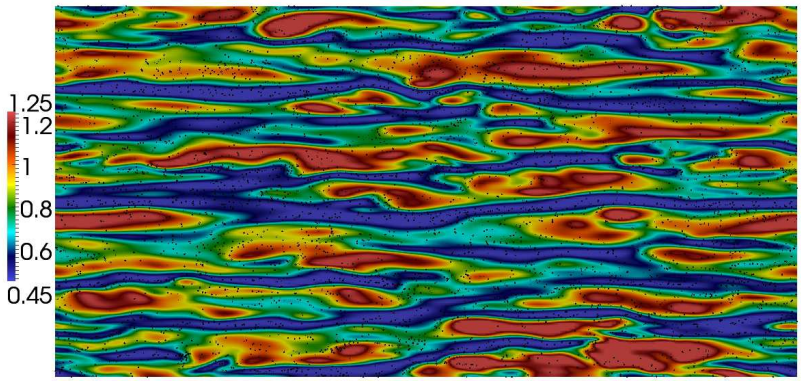

FIG. 21. The instantaneous fluid velocity (indicated by colour) in the stream-wise direction and the distribution of spherical particles with $St^+ = 5$ near the cross-sectional x-z plane at $y^+ = 8$

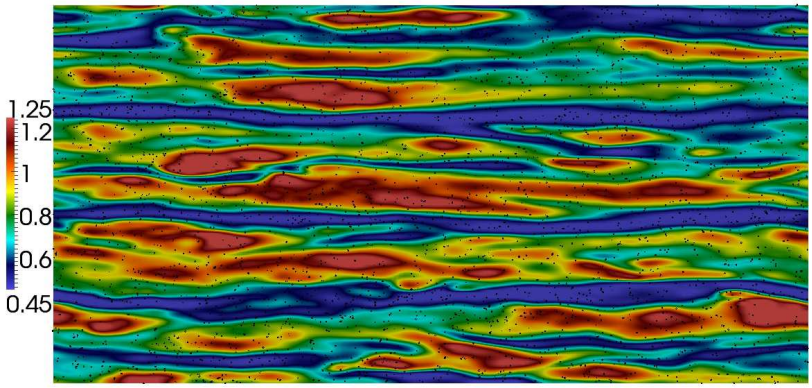

FIG. 22. The instantaneous fluid velocity (indicated by colour) in the stream-wise direction and the distribution of ellipsoids with $St^+ = 30$ and $\lambda = 5$ near the cross-sectional x-z plane at $y^+ = 8$

fluid flow in a low-speed streak slowly moves away from the wall with increasing downstream distance, but at some areas in the streak, the flow moves rapidly away from the wall. This process is referred to as lifting process[44], or known as bursting. On the other hand, the fluid flow in the large and long vortices in the high speed areas moves towards the wall, called sweeps[45]. Due to the small particle size and volume fraction, the particle distribution cannot be clearly seen in these contour plots.

Table IV shows the portion of particles and fluid flow in the low-speed areas around $y^+ = 8.0$ in the cases for various Stokes numbers and particle aspect ratios. The low-speed fluid flow accounts for around 52% to 53% in the x-z plane at $y^+ = 8.0$ in all simulations, while over 60% of the particles near the x-z plane at $y^+ = 8.0$ are found in the low-speed streaks. This indicates that particles spend more time in the low-speed streaks than in the high speed

Case with	The area of low-speed fluid flow ($u_1^f - U_1^f < 0$) at $y^+ = 8.0$	Particles in the low speed area around $y^+ = 8.0$
sphere ($St^+ = 5$ $\lambda = 1$)	53.1%	65.60%
sphere ($St^+ = 30$ $\lambda = 1$)	53.2%	65.8%
ellipsoid ($St^+ = 5$ $\lambda = 3$)	52.1%	64.75%
ellipsoid ($St^+ = 30$ $\lambda = 3$)	52.0%	64.4%
ellipsoid ($St^+ = 5$ $\lambda = 5$)	53.4%	69.4%
ellipsoid ($St^+ = 30$ $\lambda = 5$)	52.3%	59.8%

TABLE IV. The portion of particles in the low-speed streaks around $y^+ = 8.0$

zones, and this phenomena is not affected significantly by Stokes number and particle aspect ratio. This is in good agreement with Goto and Vassilicos[46] in homogeneous turbulence.

C. Particle statistics

In order to sample and analyse the statistics of the particles in the channel, the channel is divided into 100 equally spaced bins in the wall-normal direction. In which bin a particle is located is determined by the position of the center of mass.

1. Particle distribution

The ratio of the local particle volume fraction $< \alpha_y^p >$ in the wall-normal direction to the averaged particle volume fraction $< \alpha_n^p >$ of the whole channel is shown in Figs. 23 and 24 for the various cases as a function of distance to the wall. As expected, particles with high

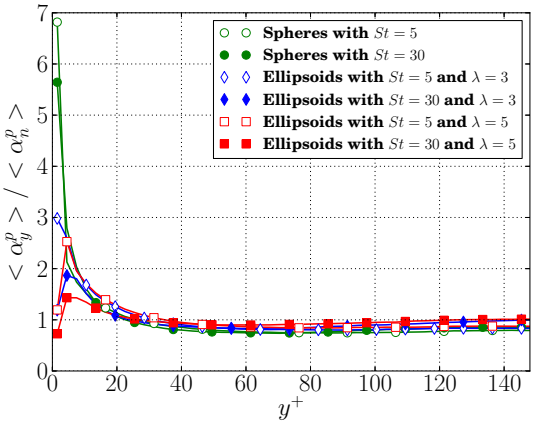

FIG. 23. The ratio of the particle volume fraction $< \alpha_y^p >$ in the wall-normal direction to averaged particle volume fraction $< \alpha_n^p >$ of the whole channel as a function of distance to the wall

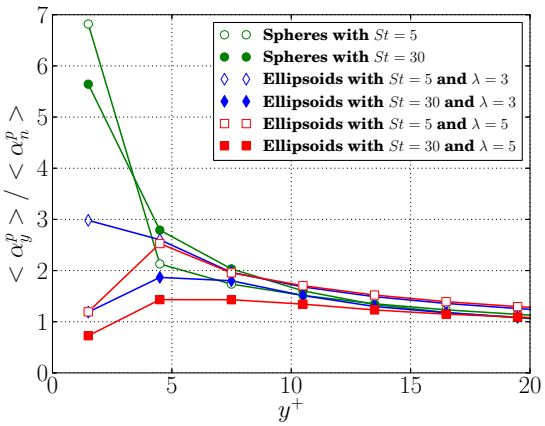

FIG. 24. The ratio of the particle volume fraction $< \alpha_y^p >$ in the wall-normal direction to averaged particle volume fraction $< \alpha_n^p >$ of the whole channel in the near wall region

inertia accumulate in the near wall region ($0 < y^+ < 10$), and the ratio $< \alpha_y^p > / < \alpha_n^p >$ peaks around $2 - 7$ close to the wall. This is because the large and long vortices sweep both the fluid and particles towards the wall, whereas the particles with relatively high inertia ($1 \ll St^+ \ll \infty$) cannot follow the fluid bursts, which rapidly move fluid away from the wall. The combination of these two effects is the main mechanism by which particles preferentially accumulate in the near wall region. In the gas-solid channel flow, not only are the fluid bursts slowed, but also the fluid sweeps are reduced since the inflow of fluid toward the wall must balance the outflow (to satisfy mass conservation). The solid particles have no such conservation law, so can accumulate. For spherical particles, the ratio reaches the largest value, 6.83 directly next to the wall for $St^+ = 5$ spheres and moderately lower to 5.54 for $St^+ = 30$. This, as noted above, is because particles with sufficiently high inertia ($St^+ = 30$) attenuate turbulence and weaken vortices. Furthermore, particles with considerably high inertia can strongly resist the effect of turbulence on them. Therefore, fewer particles with $St^+ = 30$ accumulate near the wall, compared to the case with relatively low inertia spheres ($St^+ = 5$). Next to the wall, particle-wall collisions force the mass center of ellipsoids to lie farther away from the wall than for spheres. This is because the non-sphericity of the ellipsoid hitting the wall can acquire angular momentum, whereas a sphere

can only bounce. Therefore, as can be seen from Fig. 24, the position of peak $< \alpha_y^p >$ is slightly farther from the wall for ellipsoidal particles. As the elongated shape of ellipsoids with high inertia strongly resists the effect of turbulence on the ellipsoids, the peak value of $< \alpha_y^p >$ decreases with increasing ellipsoid aspect ratio. For cases with $St^+ = 5$, the peak of the ratio decreases from 6.83 for spheres to 2.5 for ellipsoids of $\lambda = 5$, while it drops from 5.52 to 2.0 for the cases with particles of $St^+ = 30$. Small particles accumulating near the wall strongly affect the fluid turbulence in the near wall region.

2. *Particle velocity*

Fig. 25 displays particle mean velocities (U_1^{p+}) in the direction of the fluid flow for the various types of particles as a function of distance to the wall. Between $20 < y^+ < 150$, the

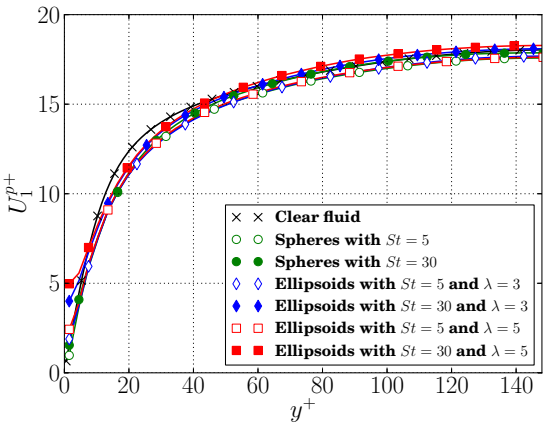

FIG. 25. Particle mean velocity in the flow direction as a function of distance to the wall

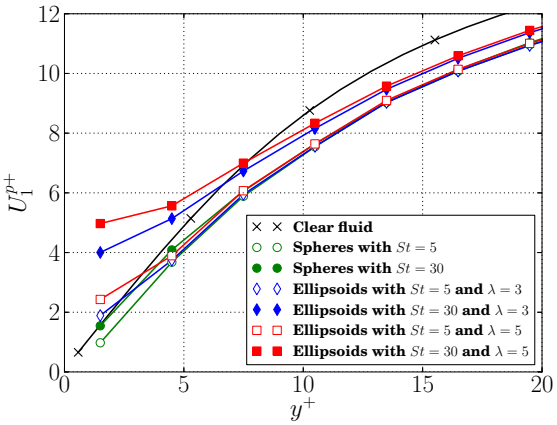

FIG. 26. Particle mean velocity in the flow direction in the near wall region

curves of U_1^{p+} in particle-laden cases are quite similar to their fluid mean velocities as shown in Fig. 2. However, in the near wall region ($0 < y^+ < 10$), particles with $St^+ = 30$ are moving on average significantly faster than the relatively low inertia particles with $St^+ = 5$, and the elongated shape also increases U_1^{p+} in the cases with the same particle inertia, as illustrated in Fig. 26.

The particle RMS velocities are shown in Figs. 27 to 29. In the near wall region ($0 < y^+ < 10$), it is clearly observed that the elongated shape of ellipsoids increases the particle velocity fluctuations. This is most likely because the collisions between non-spherical ellipsoids and

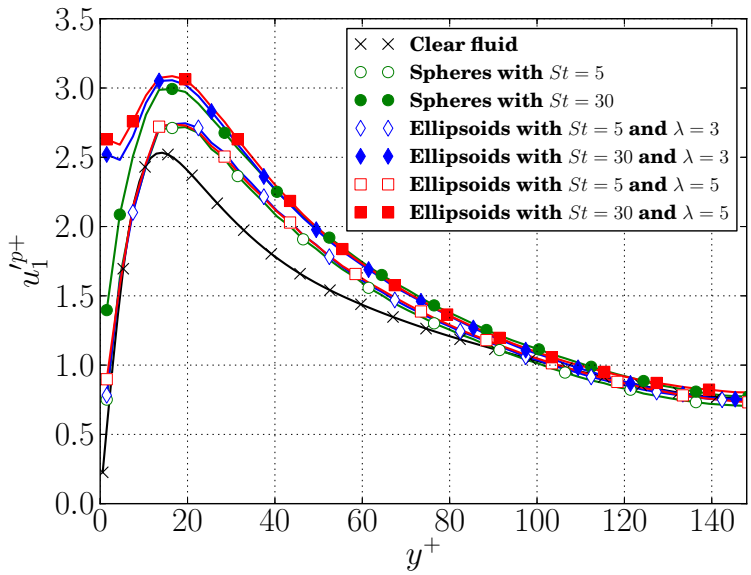

FIG. 27. Particle RMS velocity in the stream-wise direction as a function of distance to the wall

the walls increase the particle velocity fluctuations in the near wall region. Moreover, particles with high inertia (large global Stokes number) considerably strengthen this particle-wall collision effect. In the outer region ($10 < y^+ < 150$), the effect of the particle aspect ratio is quite weak, and only a slight increase in $\boldsymbol{u}_1'^{p+}$ and decrease in $\boldsymbol{u}_2'^{p+}$ and $\boldsymbol{u}_3'^{p+}$ are observed in Figs. 27 to 29. In the stream-wise direction, the large velocity gradient and slip velocity between the two phases significantly strengthen the momentum transfer, thus increasing both fluid and particle stream-wise RMS velocities. Without the effects of no-slip condition and viscosity on discrete particles, the magnitudes of particle stream-wise velocity fluctuations is significantly larger than those for the fluid phase in the outer region ($10 < y^+ < 150$), comparing Fig. 27 to Fig. 7. In the wall-normal and span-wise directions, particles with high inertia can strongly resist the effects of fluid turbulence. As a result, the particle velocity fluctuations in these two directions are much smaller than the fluid fluctuations between $10 < y^+ < 150$. As expected, these phenomena are considerably enhanced with increasing particle inertia.

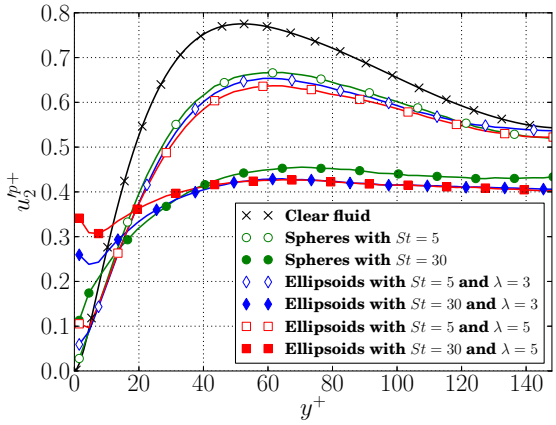

FIG. 28. Particle RMS velocity in the wall-normal direction as a function of distance to the wall

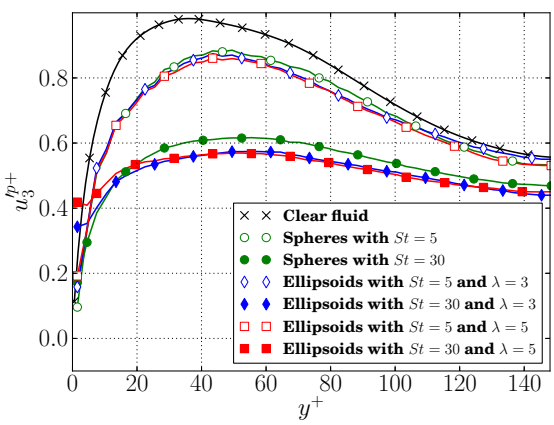

FIG. 29. Particle RMS velocity in the span-wise direction as a function of distance to the wall

3. Velocity correlation coefficients between fluid and particle phases

The relationship between the fluid flow velocities and particle velocities plays an important role in determining the interactions between the two phases. Figs. 30 and 31 show the

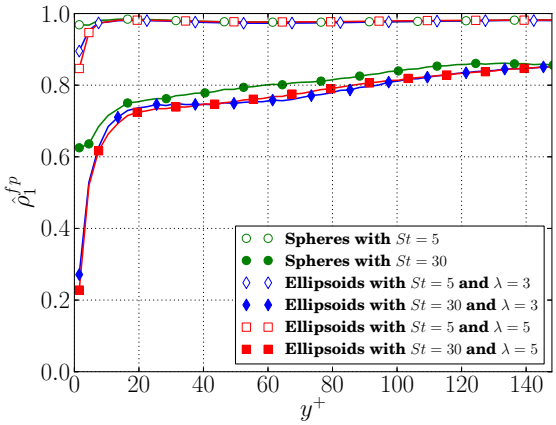

FIG. 30. The stream-wise correlation coefficient of particle and fluid velocities as a function of distance to the wall

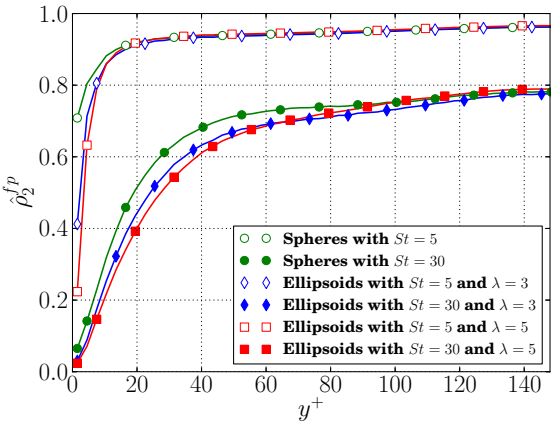

FIG. 31. The span-wise correlation coefficient of particle and fluid velocities as a function of distance to the wall

velocity correlation coefficients for the stream-wise and wall-normal directions, $\hat{\rho}_1^{fp}$ and $\hat{\rho}_2^{fp}$,

which are defined as

$$\hat{\rho}_i^{fp} = \frac{< u_i'^{f@p} u_i'^{p} >}{\left[< u_i'^{f@p2} >< u_i'^{p2} > \right]^{\frac{1}{2}}} \tag{49}$$

There are two major factors affecting the velocity correlations: particle inertia and particle collisions. Particles with high inertia have a low correlation with the flow behaviour. Therefore, the velocity correlations of particles with $St^+ = 30$ are significantly lower than those of particles with $St^+ = 5$, as shown in Figs. 30 and 31. At the wall, the particle-wall collision gives rise to complex dynamics of particles so that $\hat{\rho}^{fp}$ drops quickly in the near wall region. As the high inertia of the particles can enhance the effect of collisions, the velocity correlations resulting from the cases with particles of $St^+ = 30$ are much lower compared to cases with $St^+ = 5$ in the near wall region. Furthermore, the elongated shape of non-spherical ellipsoids tend to have a high particle-wall collision frequency and complex particle dynamics; therefore, the correlations between the particle and fluid velocities near the wall are considerably reduced with increased particle aspect ratio. Fig. 30 shows that $\hat{\rho}_1^{fp}$ in the case considering ellipsoids with $St^+ = 30$ and $\lambda = 5$ reaches a minimum around 0.229 next to the wall. As shown in Fig. 31, the effects of combining the two factors are even stronger on the span-wise velocity correlation $\hat{\rho}_2^{fp}$, which is close to zero at the wall in the cases considering ellipsoidal particles of $St^+ = 30$.

4. Mean slip velocities between the fluid flow and dispersed particles

Figs. 32 to 34 show the mean slip velocity between the fluid flow and particles in each of the three directions. Fig. 32 shows the slip velocity in the stream-wise direction. Apparently, particles add momentum to the fluid flow in the near wall region ($0 < y^+ < 20$), but obtain momentum from the flow in the outer region ($20 < y^+ < 150$). With increasing global Stokes number, the negative stream-wise slip velocity between $0 < y^+ < 20$ decreases, whereas the positive slip velocity rises in the outer region. Near the wall, the magnitude of slip velocity in the stream-wise direction rises as the particle aspect ratio increases. This arises from the complex dynamics of ellipsoids, which are caused by the particle-wall collision. However, the effect of the particle shape does not have much effect in the region between $20 < y^+ < 150$. As illustrated in Fig. 33, the mean slip velocity in wall-normal direction is almost zero in the region of $60 < y^+ < 150$, but it is positive within $0 < y^+ < 60$, peaking at 0.04

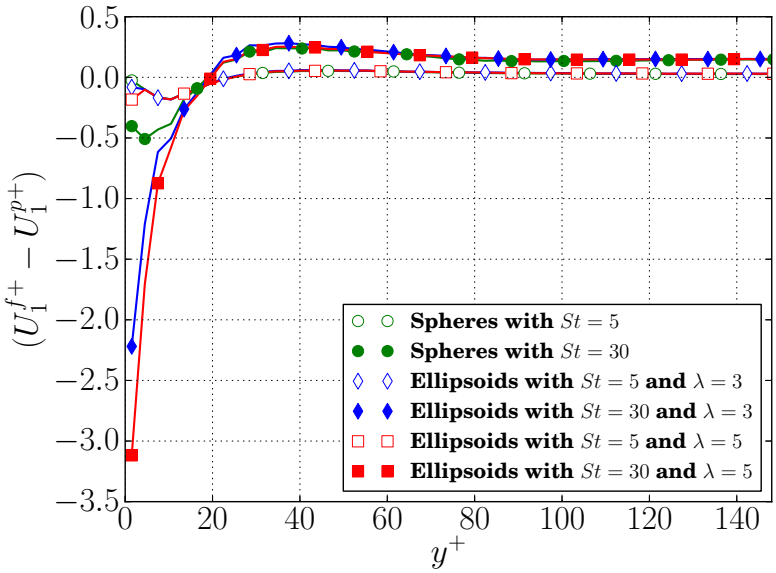

FIG. 32. Mean stream-wise slip velocity between dispersed particles and the fluid flow as a function of distance to the wall

around $y^+ = 19$. The positive wall-normal slip velocity indicates that the fluid flow sweeps

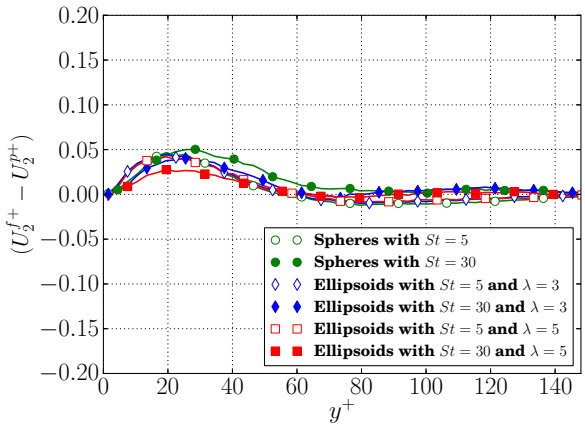

FIG. 33. Mean wall-normal slip velocity between dispersed particles and the fluid flow as a function of distance to the wall

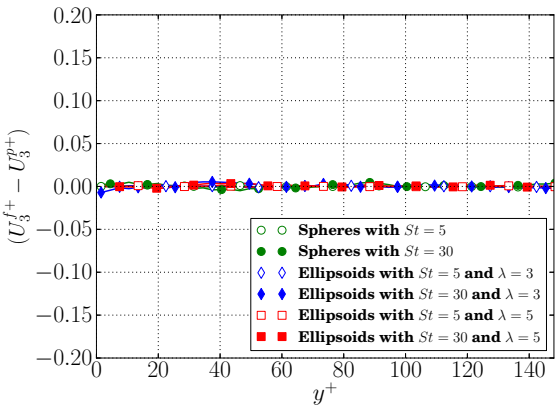

FIG. 34. Mean span-wise slip velocity between dispersed particles and the fluid flow as a function of distance to the wall

particles to the wall when particles travel to the wall, but it delays the particle when they reversely move back towards central region. These reflect the main mechanism of particle accumulation in the near wall region. It should be noted that the variance of particle inertia and aspect ratio does not influence the wall-normal slip velocity as well as the span-wise slip

velocity. Fig. 34 shows that the span-wise slip velocity is close to zero through the whole channel. Therefore, the average momentum transfer in the span-wise direction is negligible.

5. *The angular velocity of particles*

The particle angular velocity is determined by the external torques, which are caused by the hydrodynamic interactions and the collisions of particle-particle and particle-wall. As shown in Fig. 35, the magnitude of the mean span-wise angular velocity of particles

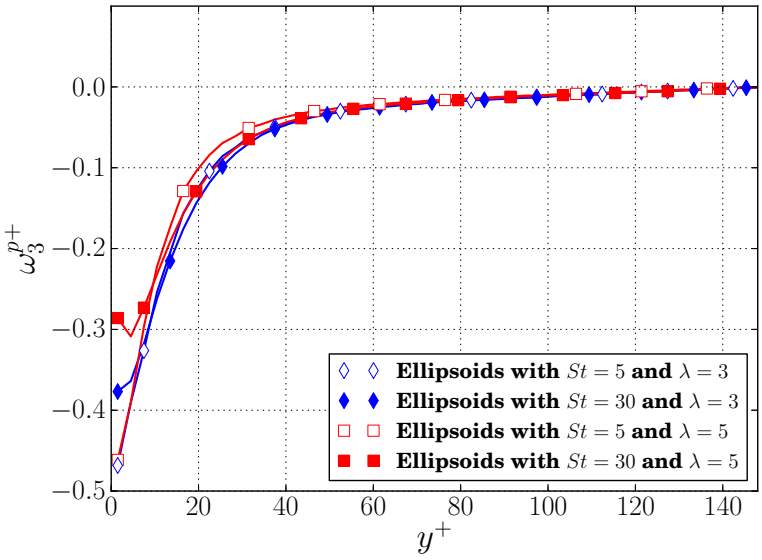

FIG. 35. The mean particle angular velocity in the span-wise direction as a function of distance to the wall

peaks at the wall, rapidly decreases to $y^+ \approx 40$ and then gradually decreases to zero at the channel center. In the near wall region ($0 < y^+ < 10$), the lighter particles ($St^+ = 5$) spin quite fast compared to heavier particles ($St^+ = 30$). This phenomena was also observed in Mortensen *et al.*[11]. The rotation of particles is determined by the hydrodynamic and collision torques. In the linear sublayer, the fluid velocity gradient has its highest value and almost has the same value for the particle-laden simulations. This gives rise to a large span-wise hydrodynamic torque in all cases. Therefore, the particles with low inertia ($St^+ = 5$) spin faster than the particles with $St^+ = 30$ in the very near wall region ($0 < y^+ < 10$). In the stream-wise and wall-normal directions, however, the particle mean angular velocities

are almost zero throughout the channel.

6. *The orientation of ellipsoidal particles*

The orientation of non-spherical particles in the channel flow strongly affects particle-fluid interactions. In previous studies[9,10,12], which neglected the effect of collisions and effects of particles on fluid flow, the particle orientation was described by the mean absolute values of direction cosines. However, the non-linear cosine function may underestimate or overestimate the interpolation of the effect of the orientation angles. Therefore, this study directly analyses the mean orientation angles (θ_i) of particles between the vector of particle major axis ($\boldsymbol{X}^p$) aligning with the x axis of body space and axes of world space, as depicted in Fig. 36. As shown from Figs. 37 to 39, all three orientation angles θ_i vary between 0° and

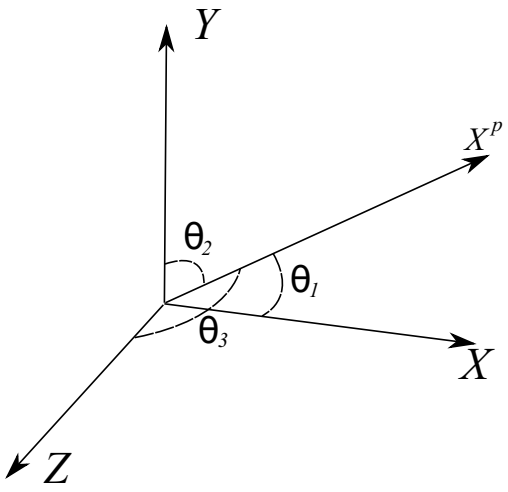

FIG. 36. Three orientation angle θ_i between three axes of world space and the vector of the ellipsoid major axis $\boldsymbol{X^p}$, which aligns with the x axis of body space, in world space.

90°, and they are correlated with each other. Moreover, their sum must always equal to 180°. As a result, a random distribution of particle orientation would lead to mean orientation angles of 60°, not the mid-value of 45°.

Fig. 37 shows that the mean angle (θ_3) in the span-wise direction peaks near the wall, between 73° and 85° for the various ellipsoids. The large value of θ_3 in the near wall region implies that the ellipsoids tend to on average align in the x-y plane and perpendicular to the span-wise direction. This phenomenon arises from the large fluid velocity gradients in the

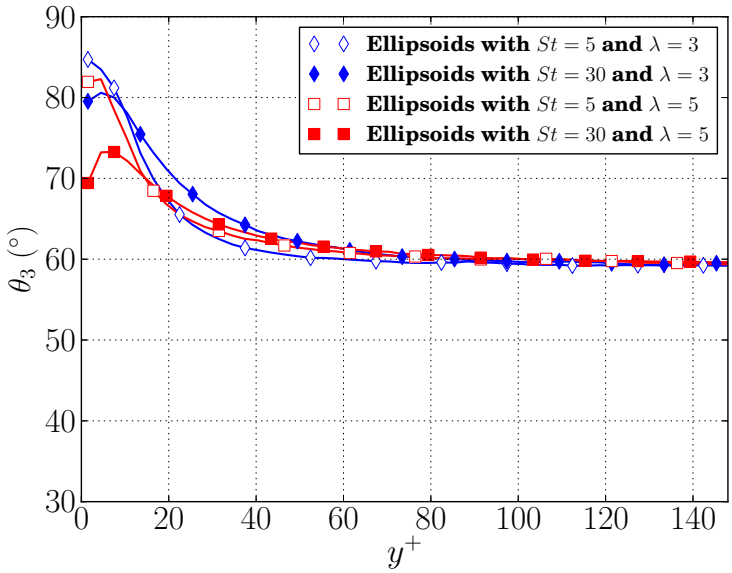

FIG. 37. Mean orientation angle θ_3 between particle major axis vector x^p and z axis of world space as a function of distance to the wall

wall-normal direction in the near wall region. Particles with high inertia are less affected by the fluid flow compared to particles with lower inertia, and thus the peak of θ_3 for ellipsoids with $St^+ = 30$ is lower than for particles with low particle inertia ($St^+ = 5$). Furthermore, increasing the aspect ratio of the ellipsoids reduces the peak of θ_3, most likely due to the more complex particle dynamics caused by the particle-wall collisions. As shown in Fig. 38, the stream-wise mean angle θ_1 of the ellipsoids reaches a minimum value in the buffer layer. As the global Stokes number rises, the minimum value of θ_1 increases. On the other hand, the mean angle θ_2 in the wall-normal direction shown in Fig. 39 peaks in the buffer layer, around $y^+ \approx 20$, for ellipsoids with $St^+ = 5$. For the $St^+ = 30$ cases, θ_2 gradually rises from the wall to the central region. It should be noted that both effects of the global Stokes number and particle aspect ratio do not influence the mean angles θ_i in the outer region ($60 < y^+ < 150$), as illustrated from Figs. 37 to 39. θ_i remains around 60° in wall-normal and span-wise directions and 53° in stream-wise direction in the central region of the channel. Although the mean angles at channel center are close to 60°, this does not suffice to conclude that the ellipsoids are randomly distributed. The distribution of these angles need to be further analysed.

The frequency of the orientation angles at different locations provides another way of

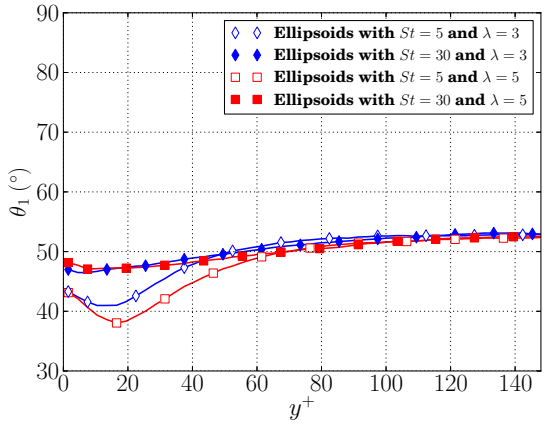

FIG. 38. Mean orientation angle θ_1 between particle major axis x^p and x axis of world space as a function of distance to the wall

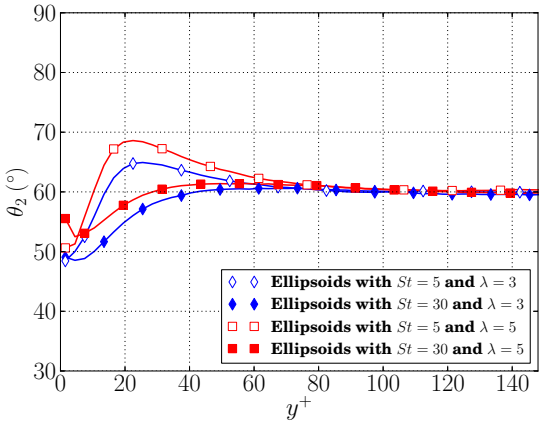

FIG. 39. Mean orientation angle θ_2 between particle major axis x^p and y axis of world space as a function of distance to the wall

analysing the orientation of particles by directly showing how orientation angles are distributed at a particular position in the channel. To precisely analyse the orientation of ellipsoidal particles, another method is proposed here. The particle major axis vector $\boldsymbol{x}^p$, can be projected on three planes: y-z, x-z and x-y planes, which are the planes perpendicular to the x, y and z axis of world space, respectively. In each plane, the orientation of each 2-D projected vector x^p_{jk} can be represented by an angle, ψ_i, between the projected vector and one axis of world space, as depicted in Fig. 40. ψ_i varies between 0° and 180° and can be expressed as

$$\begin{aligned} \psi_1 &= \arctan\left(X^p_y / X^p_z\right) \\ \psi_2 &= \arctan\left(X^p_z / X^p_x\right) \\ \psi_3 &= \arctan\left(X^p_y / X^p_x\right) \end{aligned} \tag{50}$$

Although ψ_i only represents the orientation of the projected 2-D vector and loses one degree of the particle orientation, the three components ψ_i together contain all information of the complete particle orientation. Unlike the angle θ_i, three ψ_i are not directly correlated; therefore, their distributions represent the orientation of the ellipsoids.

Figs. 41 to 43 show the pdfs of all three angles ψ_i in the near wall region ($0 < y^+ < 10$). In Fig. 41, the highest probability of ψ_1 is found at 90°, *i.e.* the particles typically align with the y direction, while the highest probability of ψ_2 shown in Fig. 42 is at 0° and 180°, *i.e.* the particles aligns with the x direction. These results are consistent with the result of the

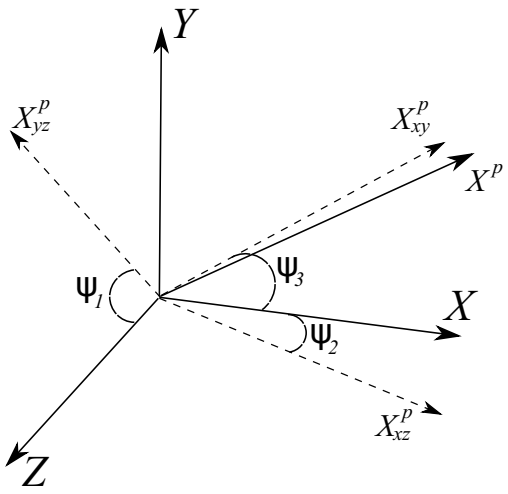

FIG. 40. The particle major axis $\boldsymbol{x}^p$ projects on the y-z, x-z and x-y planes, leading to three 2-D vectors x^p_{yz}, x^p_{xz} and x^p_{xy}. The angles ψ_i represent the angles between the 2-D vectors x^p_{yz}, x^p_{xz} and x^p_{xy} and the z, x and x axes of world space.

mean span-wise angle, θ_3, as presented in Fig. 37 and confirm that ellipsoids tend to align in the x-y plane in the near wall region. The distribution of ψ_3 in Fig. 43 indicates that the orientation of particles seems to be randomly distributed in the x-y plane near the wall. As shown in Figs. 44 to 46, the distribution of ψ_1 at the channel center is almost uniform, and the probabilities of ψ_2 and ψ_3 are distributed in very narrow region between 0.02 and 0.03. These results imply that there is no preferential orientation of particles in the central

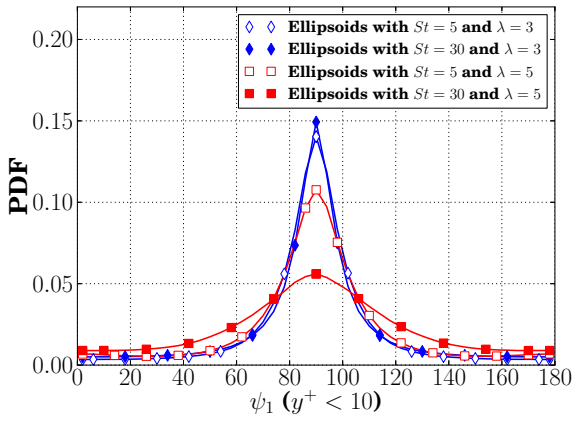

FIG. 41. The distribution of ψ_1 in the near wall region ($y^+ < 10$).

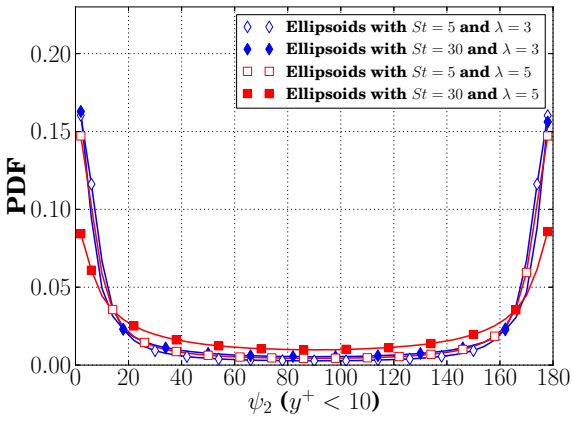

FIG. 42. The distribution of ψ_2 in the near wall region ($y^+ < 10$).

region of the channel and the orientation of particles is almost randomly distributed. It

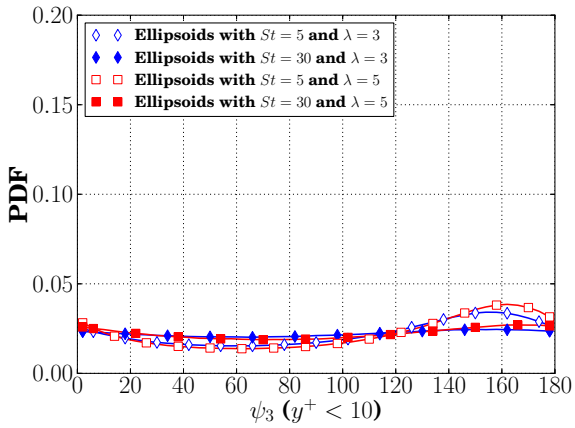

FIG. 43. The distribution of ψ_3 in the near wall region ($y^+ < 10$).

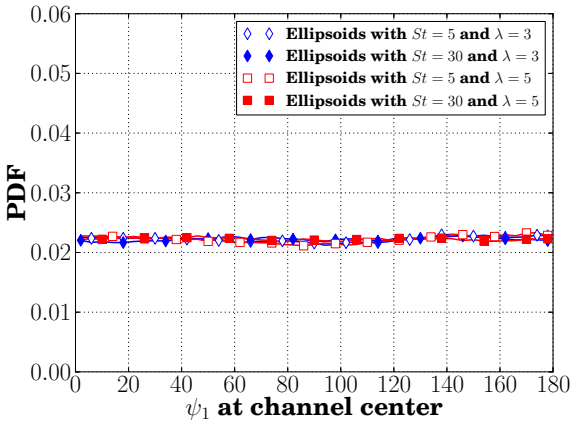

FIG. 44. The distribution of ψ_1 at channel center.

should be also noted that the pdfs of the angle ψ_3 are not symmetric in the near wall region ($0 < y^+ < 10$) as shown in Fig. 43. Figs. 47 and 48 show an ellipsoidal particle next

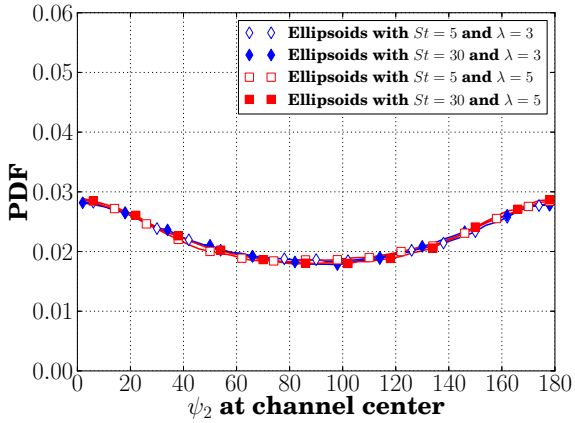

FIG. 45. The distribution of ψ_2 at channel center.

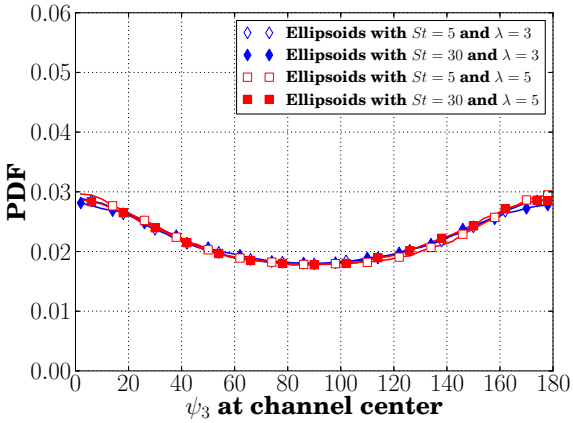

FIG. 46. The distribution of ψ_3 at channel center

to the wall near with ψ_3 less than 90° and ψ_3 more than 90°, respectively. In these two figures, the particle angular velocities ω_3^p are negative in the near wall region as presented in Fig.37. However, the effects of particle-wall collisions are opposite for the two ellipsoid with two different orientation in Figs. 47 and 48. As illustrated in Fig. 47, the collisional torque is negative and increases the magnitude of the particle angular velocity in the span-

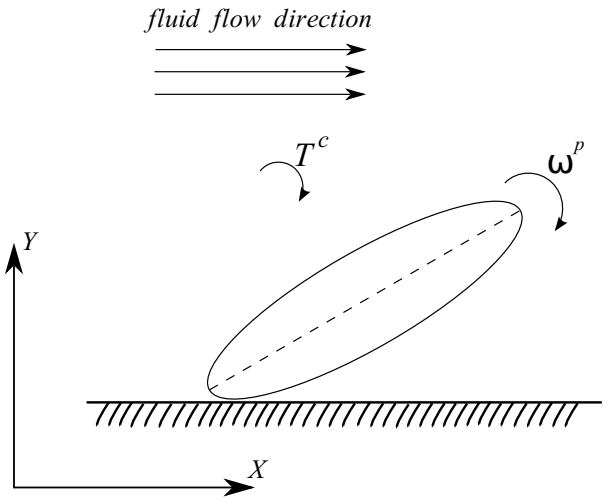

FIG. 47. An ellipsoidal particle with ψ_3 less than 90° next to the wall

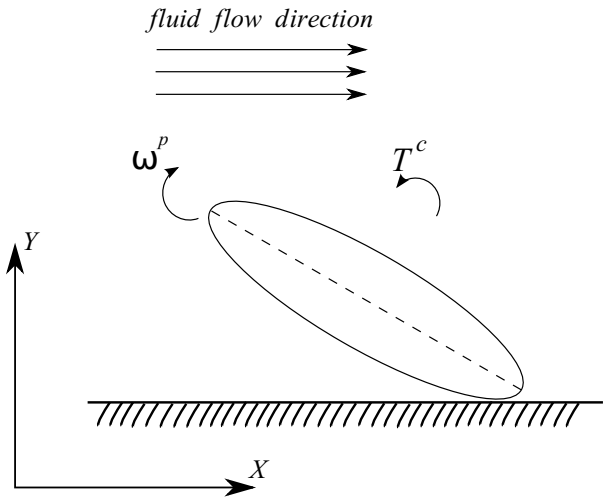

FIG. 48. An ellipsoidal particle with ψ_3 more than 90° next to the wall

wise direction when ψ_3 is less than 90°. The positive torque reduces the magnitude of the particle angular velocity when is ψ_3 more than 90° in Fig. 48. The effect of particle-wall collisions causes the asymmetric distribution of ψ_3 for cases with low global Stokes number ($St^+ = 5$) in Fig. 43, and slightly large distribution of ψ_3 between 90° and 180° in the near wall region can be observed.

V. CONCLUSION

Gas-solid turbulent flows are encountered in many industrial applications such as pneumatic conveying, combustion of coal and bio-mass, drug delivery systems, gassification and nuclear reactors, to name only a few. In most of these applications, particle shape and size play an important role. This paper investigates the effects of particle shape and Stokes number on the behaviour of non-spherical particles in turbulent channel flow. By maintaining a constant pressure difference down the channel the wall shear stress was also maintained constant, so differences in drag show up as an increase in the centerline velocities. The current study expands the one-way coupling studies[9,11,12] and investigates the effects of particle shape and global Stokes number on the both fluid flow and dispersed particles. By applying the soft-sphere collision model, all particle collisions are directly detected and their effects are resolved. Furthermore, a novel Quaternion integration method used in these simulations determines the rotation and orientation of particles and avoids the need of less accurate

rotation matrices.

The fluid statistics resulting from the simulations confirm that the presence of ellipsoidal particles with high particle inertia (large Stokes number) and large particle aspect ratio considerably attenuates the flow turbulence intensity. This is because the particles with high inertia cannot respond quickly enough to the behaviour of the fluid flow, thereby delaying the fluid flow and reducing the flow turbulence intensity. In the cases with the same large Stokes number, the elongated shape of ellipsoids further strengthens the effect of particles on the fluid flow, and thus further decreases the flow turbulence.

In the near wall region, the magnitudes of the turbulence production ($\mathcal{P}$) and the fluid flow dissipation rate ($\tilde{\varepsilon}$) decrease significantly with increasing particle inertia and aspect ratio. The effects of particles on the three major components of $\tilde{\varepsilon}$ reflect the details of the changes of the fluid flow dissipation rate and the mean square vorticity. Although the dissipation rate caused by the coupling force from particles ε_p is extremely small in the dilute flows, the presence of particles considerably influences the fluid flow. This is because the ellipsoidal particles with high inertia and large aspect ratio change the velocity profile of the fluid and indirectly change the fluid flow dissipation rate and the turbulence production.

Due to the effect of large velocity gradient in the wall-normal direction, both particle and fluid velocity fluctuations in the stream-wise direction rise with increasing Stokes number. Without the effects of viscosity and the no-slip conditions at the walls on discrete particles, the particle RMS velocity is much higher than the fluid RMS velocity in the stream-wise direction. In the outer region between $10 < y^+ < 150$, the fluid and particle RMS velocities in the wall-normal and span-wise directions decrease with increasing Stokes number. As the response time of particles is noticeably larger than the fluid response time, the particle RMS velocities in these two directions are much lower than the fluid RMS velocities. In the near wall region ($0 < y^+ < 10$), however, particle velocity fluctuations in all three directions rise with increasing Stokes number and particle aspect ratio, due to the complex particle dynamics caused by the collisions between the wall and non-spherical ellipsoids.

It was also found that particles with high inertia preferentially accumulate in the near wall region of the channel. This is because large and slow vortices (usually referred to as "sweeps") sweep the fluid and particles towards the wall, whereas the particles with relatively high inertia ($1 \ll St^+ \ll \infty$) hardly follow the flow bursts away from the wall. Thus the particles preferentially accumulate in the low speed streaks very near the wall. With increasing Stokes

number and particle aspect ratio, however, the peak value of particle volume fraction next to the wall decreases. This is because particles with significantly high inertia and aspect ratio strongly resist the effect of turbulence on them. The results of the large stream-wise slip velocity in the case with large Stokes number imply a strong momentum transfer between the two phases in this direction. However, the mean slip velocities in the other directions are very small through the channel, and thus the momentum transfer is weak in the span-wise and wall-normal directions. Because particles with high inertia cannot respond to the behaviour of the fluid flow, the velocity correlation between particles and the fluid flow are reduced with increasing particle inertia. Very close to the wall, the particle-wall collisions lead to more complex dynamics of ellipsoids than spheres; therefore, the velocities between the ellipsoids and the fluid flow are less correlated in the near wall region than those between spherical particles and the fluid flow.

The results for the orientation angle θ_i show that ellipsoidal particles tend to align in the x-y plane and perpendicular to the span-wise direction in the near wall region. The reason for this is not clear, but is most likely caused by the fluid dynamics of the boundary layer. However, since three θ_i are related to each other, it is not possible to conclude from their mean values and distributions in the central region of the channel that ellipsoids are randomly distributed at channel center, nor that they have a preferential orientation. Therefore, another orientation angle ψ_i is proposed to represent the orientation of ellipsoid. ψ_i represents the orientation of the 2-D projected particle major axis vector on the y-z, x-z, x-y planes, which perpendicular to the x, y and z axes of world space. The uniform distribution of ψ_i in the central region of the channel indicates that the orientation of particles is almost randomly distributed in the central region without any preferential orientation.

In summary, this study provides powerful evidence of turbulence reduction if small particles with large inertia and elongated shape are dispersed even in the very dilute concentrations of interest in this work. Important conclusions from this work include: the average viscosity of the flow is not affected, the average direct dissipation by the particles is negligible, and the primary mechanism by which the particles affect the flow is by altering the turbulence structure near and around the kinetic energy peak. As a final comment it must be noted that potential experiments to observe the effects as observed in this study should be very long, as the effects will only be seen at distances downstream where the particles will have reached equilibrium with the flow. For a pipe or channel we estimate that distance to be in

excess of thirty diameters after the flow itself has reached equilibrium (typically about the same distance).

ACKNOWLEDGEMENTS

The authors are grateful to the European Cooperation in Science and Technology (COST) Action FP 1005 on "*Fibre suspension flow modelling*" for the fruitful meetings and discussions. We are also grateful to Dr C. Marchioli for the fruitful discussions and access to his simulation database.

REFERENCES

[1]J. R. Fessler, J. D. Kulick, and J. K. Eaton, "Preferential concentration of heavy particles in a turbulent channel flow," Phys. Fluids **6**, 3742 (1994).

[2]J. D. Kulick, J. R. Fessler, and J. K. Eaton, "Particle response and turbulence modification in fully developed channel flow," J. Fluid Mech. **277**, 109–134 (1994).

[3]J. Kussin and M. Sommerfeld, "Experimental studies on particle behaviour and turbulence modification in horizontal channel flow with different wall roughness," Exp. Fluids **33**, 143–159 (2002).

[4]S. Lain, M. Sommerfeld, and J. Kussin, "Experimental studies and modelling of four-way coupling in particle-laden horizontal channel flow," Int. J. Heat Fluid Flow **23**, 647–656 (2002).

[5]D. Eskin, "Modeling dilute gas-particle flows in horizontal channels with different wall roughness," Chem. Eng. Sci. **60**, 655–663 (2005).

[6]C. Marchioli, A. Soldati, J. G. M. Kuerten, B. Arcen, A. Taniere, G. Goldensoph, K. D. Squires, M. F. Cargnelutti, and L. M. Portela, "Statistics of particle dispersion in direct numerical simulations of wall-bounded turbulence: Results of an international collaborative benchmark test," Int. J. Multiph. Flow **34**, 879–893 (2008).

[7]Y. Tsuji, T. Tanaka, and T. Ishida, "Lagrangian numerical simulation of plug flow of cohesionless particles in a horizontal pipe," Powder Technol. **71**, 239–250 (1992).

[8]F.-G. Fan and G. Ahmadi, "A sublayer model for wall deposition of ellipsoidal particles in turbulent streams," J. Aerosol Sci. **26**, 813–840 (1995).

[9]C. Marchioli, M. Fantoni, and A. Soldati, "Orientation, distribution, and deposition of elongated, inertial fibers in turbulent channel flow," Phys. Fluids **22**, 033301 (2010).

[10]P. Mortensen, H. Andersson, J. Gillissen, and B. Boersma, "On the orientation of ellipsoidal particles in a turbulent shear flow," Int. J. Multiph. Flow **34**, 678–683 (2008).

[11]P. H. Mortensen, H. I. Andersson, J. J. J. Gillissen, and B. J. Boersma, "Dynamics of prolate ellipsoidal particles in a turbulent channel flow," Phys. Fluids **20**, 093302 (2008).

[12]H. Zhang, G. Ahmadi, F.-G. Fan, and J. B. McLaughlin, "Ellipsoidal particles transport and deposition in turbulent channel flows," Int. J. Multiph. Flow **27**, 971–1009 (2001).

[13]L. Zhao and H. I. Andersson, "On particle spin in two-way coupled turbulent channel flow simulations," Phys. Fluids **23**, 093302 (2011).

[14]F. Zhao and B. van Wachem, "Direct numerical simulation of ellipsoidal particles in turbulent channel flow," Acta Mech. **224**, 2331 – 2358 (2013).

[15]S. Balachandar and J. K. Eaton, "Turbulent Dispersed Multiphase Flow," Annu. Rev. Fluid Mech. **42**, 111–133 (2010).

[16]C. T. Crowe, M. P. Sharma, and D. E. Stock, "The Particle-Source-In Cell (PSI-CELL) Model for Gas-Droplet Flows," J. Fluids Eng. **99**, 325–333 (1977).

[17]J. K. Eaton, "Two-way coupled turbulence simulations of gas-particle flows using point-particle tracking," Int. J. Multiph. Flow **35**, 792–800 (2009).

[18]L. Portela and R. Oliemans, "Eulerian - Lagrangian DNS/LES of particle - turbulence interactions in wall-bounded flows," Int. J. Numer. Methods Fluids **43**, 1045–1065 (2003).

[19]K. D. Squires and J. K. Eaton, "Preferential concentration of particles by turbulence," Phys. Fluids A Fluid Dyn. **3**, 1169 (1991).

[20]B. van Wachem, J. Van der Schaaf, J. Schouten, R. Krishna, and C. van den Bleek, "Experimental validation of Lagrangian-Eulerian simulations of fluidized beds," Powder Technol. **116**, 155–165 (2001).

[21]G. B. Jeffery, "The motion of ellipsoidal particles immersed in a viscous fluid," Proc. R. Soc. London. Ser. A, Contain. Pap. a Math. Phys. Character **102**, 161–179 (1922).

[22]H. Brenner, "The Stokes resistance of an arbitrary particle," Chem. Eng. Sci. **18**, 1–25 (1963).

[23]H. Brenner, "The Stokes resistance of an arbitrary particle-IV Arbitrary fields of flow," Chem. Eng. Sci. **19**, 631–651 (1964).

[24]I. Gallily and A.-H. A. Cohen, "On the orderly nature of the motion of nonspherical aerosol particles. II. Inertial collision between a spherical large droplet and an axially symmetrical elongated particle," J. Colloid Interface Sci. **68**, 338–356 (1979).

[25]H. I. Andersson, L. Zhao, and M. Barri, "Torque-coupling and particle-turbulence interactions," J. Fluid Mech. **696**, 319–329 (2012).

[26]F. Zhao and B. van Wachem, "A novel Quaternion integration approach for describing the behaviour of non-spherical particles," Acta Mech. **224**, 3091–3109 (2013).

[27]S. Elghobashi and G. C. Truesdell, "On the two-way interaction between homogeneous turbulence and dispersed solid particles. I: Turbulence modification," Phys. Fluids A **5**, 1790 (1993).

[28]C. T. Crowe, M. Sommerfeld, and Y. Tsuji, *Multiphase Flows with Droplets and Particles* (CRC Press, 1998).

[29]M. R. Maxey and J. R. J. Riley, "Equation of motion for a small rigid sphere in a nonuniform flow," Phys. Fluids **26**, 883 (1983).

[30]M. P. Allen and D. J. Tildesley, *The Computer Simulation of Liquids, Vol 42* (Oxford University Press, 1989).

[31]D. Evans and S. Murad, "Singularity free algorithm for molecular dynamics simulation of rigid polyatomics," Mol. Phys. **34**, 327–331 (1977).

[32]L. Ibanez, "Tutorial on Quaternions Part I," Tech. Rep. 8 (Insight Segmentation and Registration Toolkit, ITK, 2001).

[33]M. Kleppmann, "Simulation of colliding constrained rigid bodies," Tech. Rep. 683 (University of Cambridge, UCAM-CL-TR-683, ISSN 1476-2986, 2007).

[34]O. R. Walton and R. L. Braun, "Simulation of rotary-drum and repose tests for frictional spheres and rigid sphere clusters," DOE/NSF Work. Flow Part. (1993).

[35]P. K. Yeung and S. B. Pope, "An algorithm for tracking fluid particles in numerical simulations of homogeneous turbulence," J. Comput. Phys. **79**, 373–416 (1988).

[36]R. D. Mindlin and H. Deresiewicz, "Elastic spheres in contact under varying oblique forces," J. Appl. Mech. **20**, 327–344 (1953).

[37]G. Mallouppas and B. van Wachem, "Large Eddy Simulations of Turbulent Particle-Laden Channel Flow," Int. J. Multiph. Flow **54**, 65–75 (2013).

[38]J. Kim, P. Moin, and R. Moser, "Turbulence statistics in fully developed channel flow at low Reynolds number," J. Fluid Mech. **177**, 133–166 (1987).

[39]M. Shapiro and M. Goldenberg, "Deposition of glass fiber particles from turbulent air flow in a pipe," J. Aerosol Sci. **24**, 65–87 (1993).

[40]R. A. Antonia and J. Kim, "A numerical study of local isotropy of turbulence," Phys. Fluids **6**, 834–841 (1994).

[41]R. A. Antonia, J. Kim, and L. W. B. Browne, "Some characteristics of small-scale turbulence in a turbulent duct flow," J. Fluid Mech. **233**, 369–388 (1991).

[42]W. George and H. J. Hussein, "Locally axisymmetric turbulence," J. Fluid Mech. **233**, 1–23 (1991).

[43]J. Kim and R. A. Antonia, "Isotropy of the small scales of turbulence at low Reynolds number," J. Fluid Mech. **251**, 219–238 (1993).

[44]S. J. Kline, W. C. Reynolds, F. A. Schraub, and P. W. Runstadler, "The structure of turbulent boundary layers," J. Fluid Mech. **30**, 741–773 (1967).

[45]E. Corino and R. S. Brodkey, "A visual investigation of the wall region in turbulent flow," J. Fluid Mech. **37**, 1–30 (1969).

[46]S. Goto and J. C. Vassilicos, "Self-similar clustering of inertial particles and zero-acceleration points in fully developed two-dimensional turbulence," Phys. Fluids **18**, 115103;1–10 (2006).